Project Report on

Deep Neural Profiling Identifies RAP1GAP2 as a Latent Regulator in Head and Neck Squamous Cell Carcinoma

In partial fulfilment of the requirements of the BMB433 for the degree of Bachelor of Science in Biochemistry and Molecular Biology of the Shahjalal University of Science and Technology, Sylhet

Submitted By

Registration No: 2019433077
BSc Session: 2019-2020

Department of Biochemistry and Molecular Biology
School of Life Science
Shahjalal University of Science and Technology
Sylhet-3114, Bangladesh

Date of Submission: July 07, 2025

Acknowledgments

Foremost, I want to express my gratitude to Almighty God for the wisdom, strength, peace of mind, and good health. He bestowed upon me to complete my dissertation.

I place on record my sincere gratitude to my supervisor **Papia Rahman**, Lecturer, Department of Biochemistry and Molecular Biology, Shahjalal University of Science and Technology, Sylhet-3114, for allowing me the opportunity to enroll in my project under her kind supervision and for her patience, motivation, and immense knowledge. Her guidance helped me throughout the research and writing of this thesis. I could not have imagined having a better advisor and mentor for my project study. I am extremely thankful and indebted to her valuable guidance and encouragement.

Finally, I must express my very profound gratitude to my parents and friends for providing me with unwavering support and endless encouragement during my studies as well as during the process of researching and writing this thesis. This accomplishment would not have been possible without them.

Joy Prokash Debnath

July 07, 2025

To Whom It May Concern

I hereby certify that in accordance with the laws of Shahjalal University of Science and Technology, Sylhet-3114, Bangladesh, the project work entitled **"Deep Neural Profiling Identifies RAP1GAP2 as a Latent Regulator in Head and Neck Squamous Cell Carcinoma"** described here is entirely own work of **Joy Prokash Debnath** bearing Registration No. **2019433077**, **Session:** 2019-2020. This project does not contain any materials which were previously published or written by another person, except duly referred. The work was conducted under my supervision and was enrolled in the degree of Bachelor of Science in Biochemistry and Molecular Biology at the Shahjalal University of Science and Technology, Sylhet-3114, Bangladesh. All information provided in the project paper has been obtained and presented following academic rules and ethical guidelines.

I hereby endorse his project to be submitted for evaluation.

……

Signature of the Supervisor

Papia Rahman

Lecturer

Department of Biochemistry and Molecular Biology (BMB)

Shahjalal University of Science and Technology, Sylhet-3114, Bangladesh

Abbreviations

Abbreviation	Full Form
HNSCC	Head and Neck Squamous Cell Carcinoma
DGE	Differential Gene Expression
PCA	Principal Component Analysis
VAE	Variational Autoencoder
SBS	Sensitivity-Based Scoring
GSEA	Gene Set Enrichment Analysis
IG	Integrated Gradients
AUROC	Area Under the Receiver Operating Characteristic curve
AUPRC	Area Under the Precision–Recall Curve
KEGG	Kyoto Encyclopedia of Genes and Genomes
GO	Gene Ontology
FDR	False Discovery Rate
MLP	Multi-Layer Perceptron
ERK	Extracellular Signal-Regulated Kinase
MAPK	Mitogen-Activated Protein Kinase
MMP	Matrix Metalloproteinase
IG	Integrated Gradients
LFC	Log Fold Change
NES	Normalized Enrichment Score

Abstract

Background: Conventional differential gene expression (DGE) analysis inadequately captures the complex molecular changes that drive the progression of head and neck squamous cell carcinoma (HNSCC). Variational Autoencoder (VAE) offers a deep learning approach to uncover hidden patterns in high-dimensional transcriptomic data, potentially

Methods: Gene expression datasets were combined, from multiple databases and trained a VAE to compress the data into a small, hidden space. Integrated Gradients was utilized, an automated attribution technique, to determine the contribution of each gene to each latent node (biological representation). Genes that consistently had high attribution scores across all latent dimensions were chosen as candidate regulators. Pathway enrichment analysis and classification analyses unveiled the biological significance of these genes.

Results: The VAE learned latent features that are biologically important, and Integrated Gradients showed a group of genes that have a big impact on these features. RAP1GAP2 was consistently one of the top contributors across all 50 latent variables, which is noteworthy. RAP1GAP2 had the highest latent-space importance and strong discriminative power for distinguishing HNSCC from control samples, with a performance of 0.769. This occurred despite the lack of substantial differential expression in tumors relative to normal samples. Biological interpretation suggests that RAP1GAP2, a GTPase-activating protein that inactivates Rap1, may help tumors invade by turning off Rap1 and changing MAPK signaling and Golgi-mediated secretion.

Conclusion: Our deep learning framework identified RAP1GAP2 as a latent candidate regulator in HNSCC. This demonstrates how VAE and Integrated Gradients may discover candidate regulators overlooked by alternative approaches. This method delivers novel dimensions about the biology of HNSCC tumors that could benefit future research and therapeutic approaches.

Keywords: Head and neck squamous cell carcinoma (HNSCC); transcriptomics; deep learning; latent features; RAP1GAP2; Rap1 signaling; MAPK pathway; Golgi secretion

Table of Contents

Contents Page No.

Abstract.....IV

Keywords:.....IV

List of Tables.....VII

List of Figures.....VII

Introduction.....9

1.1 Overview of Head and Neck Squamous Cell Carcinoma.....1

1.2 Complexity of Cancer Biology and Analytical Gaps.....2

1.3 Deep Learning for Latent Feature Discovery.....2

1.4 Gene Attribution with Integrated Gradients.....4

1.5 Revealing a Latent Candidate Regulator: The Case of *RAP1GAP2*.....5

1.6 Hypothesis of the Study.....6

1.7 Significance of the Study.....6

1.8 Aims and Objective.....6

Material and Methods.....8

2.1 Workflow of the Study.....8

2.2 Datasets Retrieval.....8

2.3 Data Integration, Batch Effect Removal and Preprocessing.....11

2.4 Training Deep Neural Network Models.....12

2.4.1 Datasets Merging and Standardization.....12

2.4.2 Traditional Deep Learning Model.....12

2.4.3 Additional Sample Distribution.....13

2.5 Neural Network Design and Hyperparameter Optimization.....13

2.5.1 Train Model with Adam Optimizer.....13

2.5.2 Cross validate and Extract Best Latent Dimension.....13

2.6 Learning Robust Latent Representations.....14

2.7 Gene Attribution and Pathway Analysis.....14

2.7.1 Sensitivity-Based Scoring (SBS) for Gene-to-Latent Attribution.....14

2.7.2 Pathway Enrichment Analysis of Latent Variable-Associated Genes.....14

2.7.3 Gene Set Enrichment Analysis (GSEA) 15
2.8 Supervised Deep Learning Model Training 15
2.8.1 Gene Selection and Data Collection 15
2.8.2 Normalization and Batch Correction 15
2.8.3 Model Development and Training 16
2.8.4 Evaluation and Visualization 16
2.9 Differential Gene Expression analysis 16
Result **17**
3.1 Data Preprocessing and Quality Assessment 16
3.2 Latent Space Extraction Using Deep Neural Network 17
3.3 Latent Variables Capture Distinct Gene Programs and Biological Pathways 18
3.4 Functional Characterization of Latent Variables via GSEA 20
3.5 Deep Learning-Based Classification of Candidate Genes in HNSCC 23
3.6 RAP1GAP2 Emerges as the Most Predictive Gene in Single-Feature Classification Models 23
3.7 RAP1GAP2 Emerges as a Latent Candidate Regulator Despite Non-Significance in Differential Expression Analysis 27
Discussion **28**
4.1 Discussion 28
4.2 Limitations of the Study 31
4.3 Future Directions 32
5. Conclusion **34**
References **34**
Appendices **38**
Selected Latent Variable-Enriched Pathways **40**
GSEA Info for Top 50 Pathways **41**

List of Tables

SL. NO.	Table Captions	Page No.
Table 2.1	Expression Profiling Datasets for Head and Neck Cancer	9
Table 3.1	Performance metrics for single-gene classification models	24

List of Figures

SL. NO.	Figure Captions	Page No.
Figure 1.1	Anatomical regions of the head and neck involved in cancer.	1
Figure 1.2	Basic architecture of a deep neural network.	3
Figure 2.1	Overview of the study pipeline	8
Figure 3.1	Preprocessing and PCA of gene expression data	16
Figure 3.2	Model Performance and Gene Attribution	18
Figure 3.3	Interpretation of latent variables via gene attribution and enrichment	19
Figure 3.4	Pathway enrichment heatmap using GSEA	21
Figure 3.5	Identification of candidate genes and classification performance	23
Figure 3.6	RAP1GAP2 as a predictive gene for HNSCC classification	26

Figure 3.7	RAP1GAP2 as a latent candidate regulator despite non-significance in DGE	26
Figure 4.1	Mechanistic role of RAP1GAP2 in HNSCC invasion and metastasis	30

Chapter One

Introduction

1.1 Overview of Head and Neck Squamous Cell Carcinoma

Head and neck squamous cell carcinoma (HNSCC) is of particular clinical significance because human papillomavirus (HPV) infection has driven a rise in its incidence in recent decades, mainly in tumors of the oropharynx, making HPV-positive HNSCC one of the fastest-growing cancers in many high-income nations (Lechner et al. 2022). An anatomical illustration of the oropharynx and its neighboring regions is shown in **Figure 1.1** to highlight the tumor's location and clinical context.

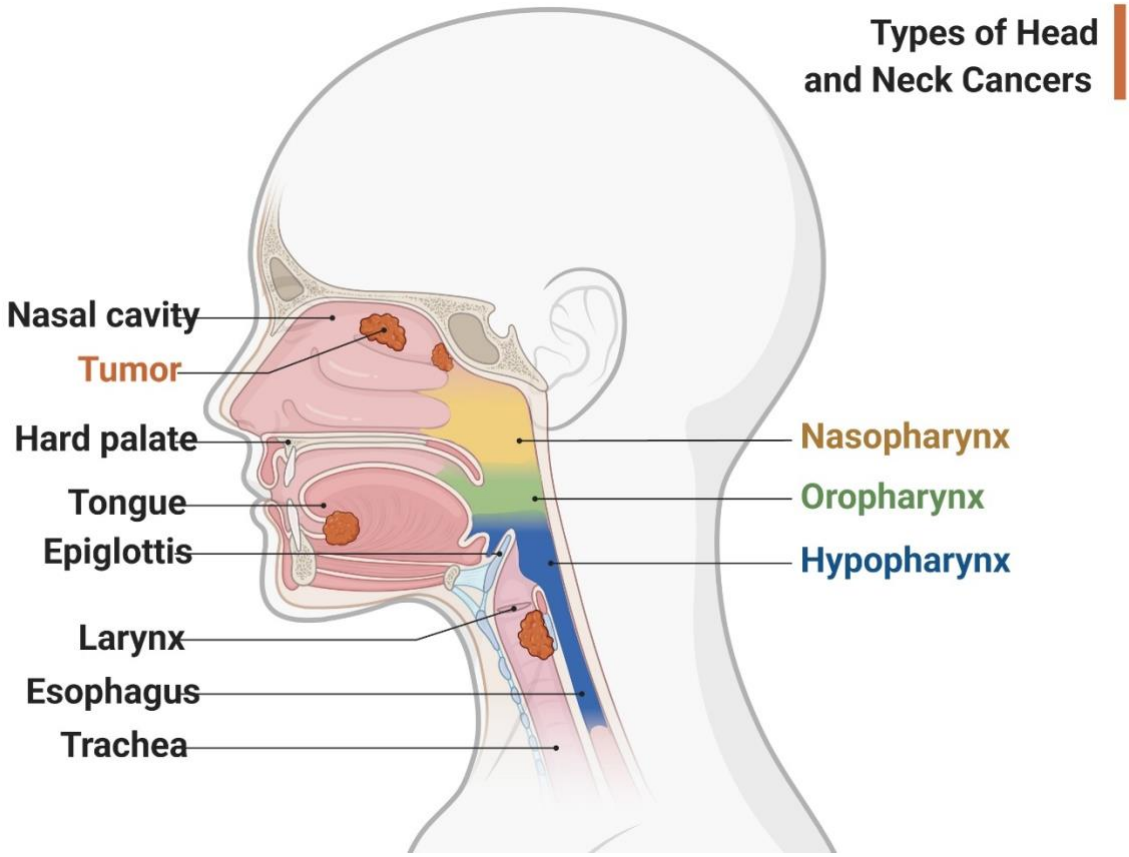


Figure 1.1 Anatomical regions of the head and neck involved in cancer. [Figure created using Adobe Illustrator v27.8.1].

Because of its subtle early symptoms, HNSCC frequently manifests at advanced stages, leading to substantial morbidity and mortality. Therefore, a deeper comprehension of the molecular foundations of HNSCC is urgently needed to facilitate earlier detection, better patient stratification, and more successful precision therapies (Sabbatini and Manganaro 2023). Results for advanced HNSCC are still uncertain despite advancements in systemic treatments, radiation therapy, and surgery. Gaining a better understanding of the

transcriptome landscape of the tumor may help identify new molecular drivers that could enhance patient care.

1.2 Complexity of Cancer Biology and Analytical Gaps

The biology of cancer is extraordinarily complex, involving non-linear interactions among genes and pathways that drive tumor behavior. Traditional differential gene expression (DGE) analysis—which typically relies on linear models or statistical tests to find genes individually up- or down-regulated in tumors—has clear limitations when faced with this complexity. DGE methods excel at identifying genes with large average expression changes, but they may overlook genes that exert their effects through subtle or combinatorial patterns.

In other words, patient subgroups or tumor phenotypes could be determined by gene sets that do not show obvious one-at-a-time differences and thus remain "invisible" to linear DGE approaches (Rampášek et al. 2019). Indeed, recent work has cautioned that when nonlinear machine learning models identify patient groupings, the defining gene signatures might be missed by conventional DGE due to its linear nature (Rampášek et al. 2019).

Such underappreciated genes or gene interactions may be crucial for the development of cancer, making this gap problematic. Analytical techniques that can capture the nonlinear dependencies in gene expression data and go beyond linear assumptions are required. One potential remedy is explainable algorithms (machine learning), which can reveal multivariate gene patterns that would otherwise go unnoticed by applying interpretability techniques to complex models (Abbas and El-Manzalawy 2020; Way et al. 2020). In conclusion, techniques that can model and explain the complex, nonlinear relationships that define cancer biology are necessary to overcome the shortcomings of DGE.

1.3 Deep Learning for Latent Feature Discovery

We use deep learning—more especially, unsupervised deep neural networks—to learn biologically significant latent variables from transcriptomic data in order to overcome these difficulties. A class of deep generative models that are ideal for this task are Variational Autoencoder (VAE). A VAE preserves as much information as possible while compressing high-dimensional gene expression profiles into a lower-dimensional latent space. Complex gene expression patterns can be reduced by this method to a collection of latent features that capture patient variability and underlying biological signals. Figure 1.2 illustrates the basic architecture of a deep neural network, where an encoder maps gene expression into

latent representations for downstream interpretation. High-dimensional gene expression data are processed through multiple layers of an encoder network to generate low-dimensional latent features. These latent variables represent condensed biological signals and are suitable for interpretation, classification, or further modeling.

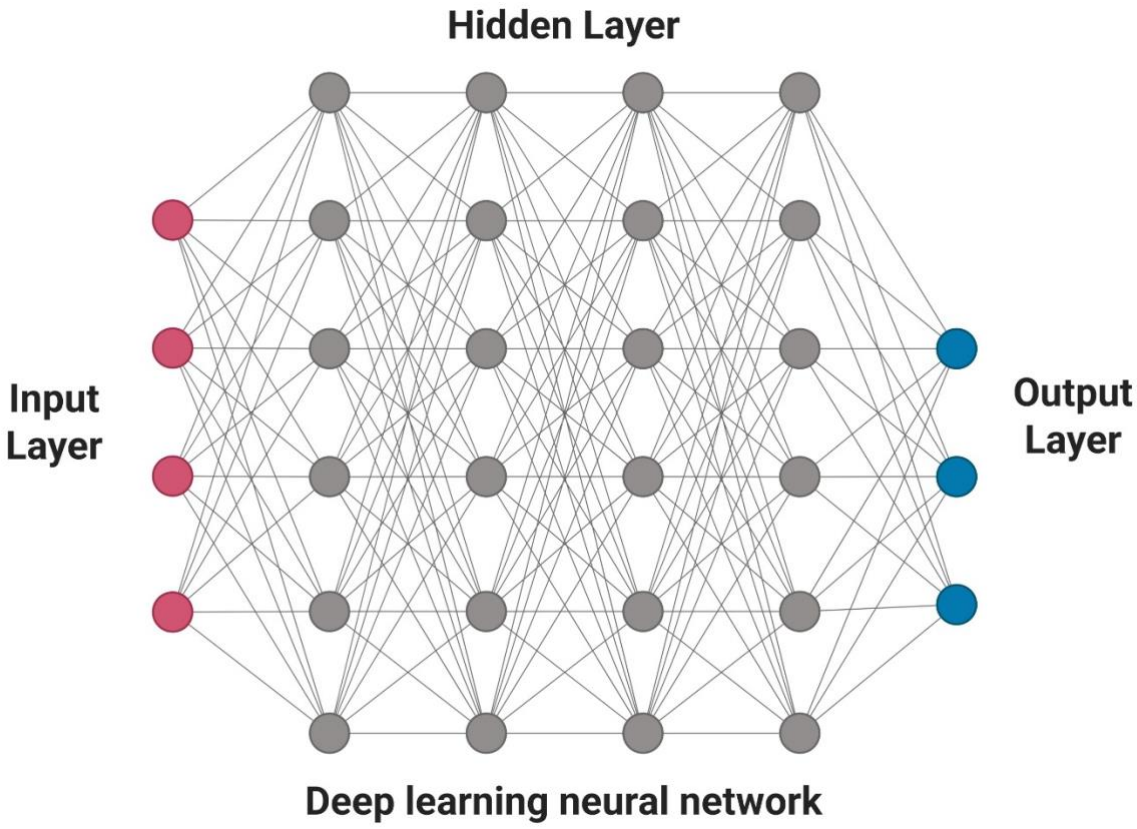


Figure 1.2 Basic architecture of a deep neural network. [Figure created using Adobe Illustrator v27.8.1].

Largescale gene expression datasets have seen the successful application of VAE and related autoencoder techniques, which have shown promise in modeling non-linear gene interactions and enhancing outcome predictions (Sundararajan et al. 2017). To illustrate the ability of deep learning to capture subtle transcriptomic effects of treatment, Rampášek et al. demonstrated that a VAE-based model ("Dr.VAE") could learn latent representations of cancer cell line expression data that improve drug response prediction (Zhang et al. 2006). Similar to this, Way et al. used VAE to compress pan cancer gene-expression data and discovered that different biological signals (like pathway activities and mutational status) emerged when the latent dimensionality was varied. This suggests that deep compression can learn complementary aspects of tumor biology that are not possible with a single linear compression or DGE analysis (Way et al. 2020). These studies underscore

that deep neural networks can extract non-linear features from gene expression data, potentially revealing patterns that are not evident to traditional methods.

However, a known drawback of deep learning models is their limited interpretability—the latent features or learned representations are "black boxes" without clear biological meaning. In the context of cancer transcriptomics, it is not enough to discover latent variables; we also need to understand which genes those variables represent or how they relate to known biology. Simply compressing data with a VAE might yield abstract features that correlate with disease, but without interpretation we cannot translate those features into testable biological insights.

1.4 Gene Attribution with Integrated Gradients

To interpret the latent space and connect it back to gene-level biology, we employ integrated gradients, a robust feature attribution method for neural networks. Integrated gradients provide a way to quantify the contribution of each input feature (in this case, each gene's expression) to a given output or latent variable in the model (Janizek et al. 2023). Formally, integrated gradients work by integrating the gradients of the model's output with respect to inputs along a path from a baseline to the actual input, yielding an attribution score for every feature that satisfies desirable axioms of fairness and sensitivity (Janizek et al. 2023). Introduced by Sundararajan et al. in 2017, this method has become a popular tool for explaining deep learning predictions in various domains (Janizek et al. 2023). In our study, we harness integrated gradients to attribute genes to latent variables learned by the VAE and to any downstream predictive outputs. This approach effectively "opens the black box" of the autoencoder by highlighting which genes most strongly influence each latent dimension of the model.

Notably, earlier studies have shown how useful it is to combine feature attribution and deep generative models in genomics. For instance, Dincer et al. identified the top contributing genes for each latent dimension by applying integrated gradients to the latent features of a VAE trained on cancer gene expression data (Janizek et al., 2023). Researchers can anchor abstract features in concrete biology by using this post hoc interpretation of latent space. For example, based on the genes with the highest attributions, a latent dimension may end up representing a pathway or cell cycle signature. Building on these concepts, we derive gene-level importance scores for the learned latent factors by combining our VAE with integrated gradients. By doing this, we can identify the genes that are most important for

differentiating HNSCC tumors from controls (or other tumor subtypes) and that account for the variation captured in the latent space. In addition to maintaining interpretability, this combination of unsupervised, deep learning and explainability techniques enables us to find biologically significant patterns that would be missed by linear analysis alone.

1.5 Revealing a Latent Candidate Regulator: The Case of *RAP1GAP2*

By using this deep learning framework on head and neck cancer transcriptomic data, new understandings of the molecular causes of the disease are revealed. Integrated gradients identify the genes that define the latent variables that the variational autoencoder extracts and that summarize gene expression patterns across tumors. Our analysis reveals that RAP1GAP2 is a latent candidate regulator in HNSCC, which is intriguing. With a high attribution score, RAP1GAP2 stands out in our model as one of the main contributors to a latent feature that is very predictive of the presence of HNSCC. This finding is noteworthy because, according to standard differential expression analysis, RAP1GAP2 was not identified as significant; that is, its average expression levels between tumor and normal do not differ sufficiently to meet standard statistical thresholds. RAP1GAP2 would have been completely overlooked by traditional DGE, but our deep learning method revealed it to be a significant participant with a nonlinear contribution to the tumor transcriptome. The impact of RAP1GAP2 only becomes apparent when taking into account intricate interactions recorded in the latent space, demonstrating how deep learning can uncover latent candidate genes that elude linear analysis.

From a biological standpoint, the implication of RAP1GAP2 in HNSCC is plausible and generates new hypotheses. Although RAP1GAP2 itself has not been well studied in HNSCC, it belongs to the same family as Rap1GAP (also known as RAP1GAP1), which has been reported to act as a tumor suppressor in HNSCC: in oropharyngeal tumor models, restoring Rap1GAP expression reduced active Rap1 signaling and slowed tumor growth in vivo (Zhang et al. 2006). This prior evidence of the Rap1 pathway's involvement in HNSCC provides context for our findings: it suggests that downregulation or dysregulation of Rap1-inhibitory proteins (like Rap1GAP or RAP1GAP2) could contribute to oncogenic processes in HNSCC. Our identification of RAP1GAP2 as a latent candidate regulator, despite its subtle expression changes, underscores how deep learning-based analysis can pinpoint functionally relevant genes that conventional analyses deem insignificant. Such genes might represent early changes or context specific vulnerabilities that are missed when focusing only on large fold-changes. Identifying RAP1GAP2 as highly predictive of

HNSCC opens the door to further experimental validation and investigation into its potential role in tumor suppression or as a biomarker for disease presence.

1.6 Hypothesis of the Study

We hypothesize that deep neural networks, particularly Variational Autoencoder (VAE) models, can learn latent representations of transcriptomic data that capture complex, nonlinear biological signals associated with HNSCC. These latent features are expected to reveal candidate molecular regulators that conventional differential gene expression (DGE) analyses may overlook due to their reliance on linear assumptions. By integrating unsupervised deep learning with interpretability techniques such as integrated gradients, we anticipate uncovering key gene-level contributors—such as RAP1GAP2—that may contribute to tumor invasion and progression despite showing no significant differential expression. This approach offers a novel avenue for identifying biologically relevant signals embedded in high-dimensional gene expression data.

1.7 Significance of the Study

Comprehending the molecular pathways underlying HNSCC is a significant challenge, especially due to the constraints of conventional gene expression analysis techniques that frequently depend on linear assumptions. This paper presents a deep learning system that may reveal nonlinear and concealed transcriptome signals, providing an innovative method for identifying candidate genes in HNSCC. Utilizing variational autoencoders and integrated gradients, we discovered RAP1GAP2 as an unknown factor in tumor invasion and development, despite its absence of differential expression according to traditional statistical standards. This underscores the capability of modern computational modeling to not only augment but also exceed conventional analytical methods. The results of this study provide novel avenues for biological research and therapeutic development in HNSCC and create a framework for the application of interpretable deep learning to other intricate diseases.

1.8 Aims and Objective

This study aims to uncover hidden transcriptomic patterns and identify candidate gene-level regulators of HNSCC by applying deep neural network-based methods—specifically variational autoencoders and integrated gradients—that go beyond the limitations of traditional differential expression analysis.

Objectives of the study are,

- To apply deep learning (VAE) for compressing gene expression into latent features.
- To detect complex, nonlinear gene patterns missed by standard tools.
- To interpret latent features using Integrated Gradients for gene attribution.
- To combine unsupervised modeling with supervised classification.
- To identify candidate molecular regulators potentially involved in HNSCC progression.
- To compare the performance of this method with traditional differential gene expression approaches.

Chapter Two

Material and Methods

2.1 Workflow of the Study

The design of the overall study is illustrated in **Figure 2.1**

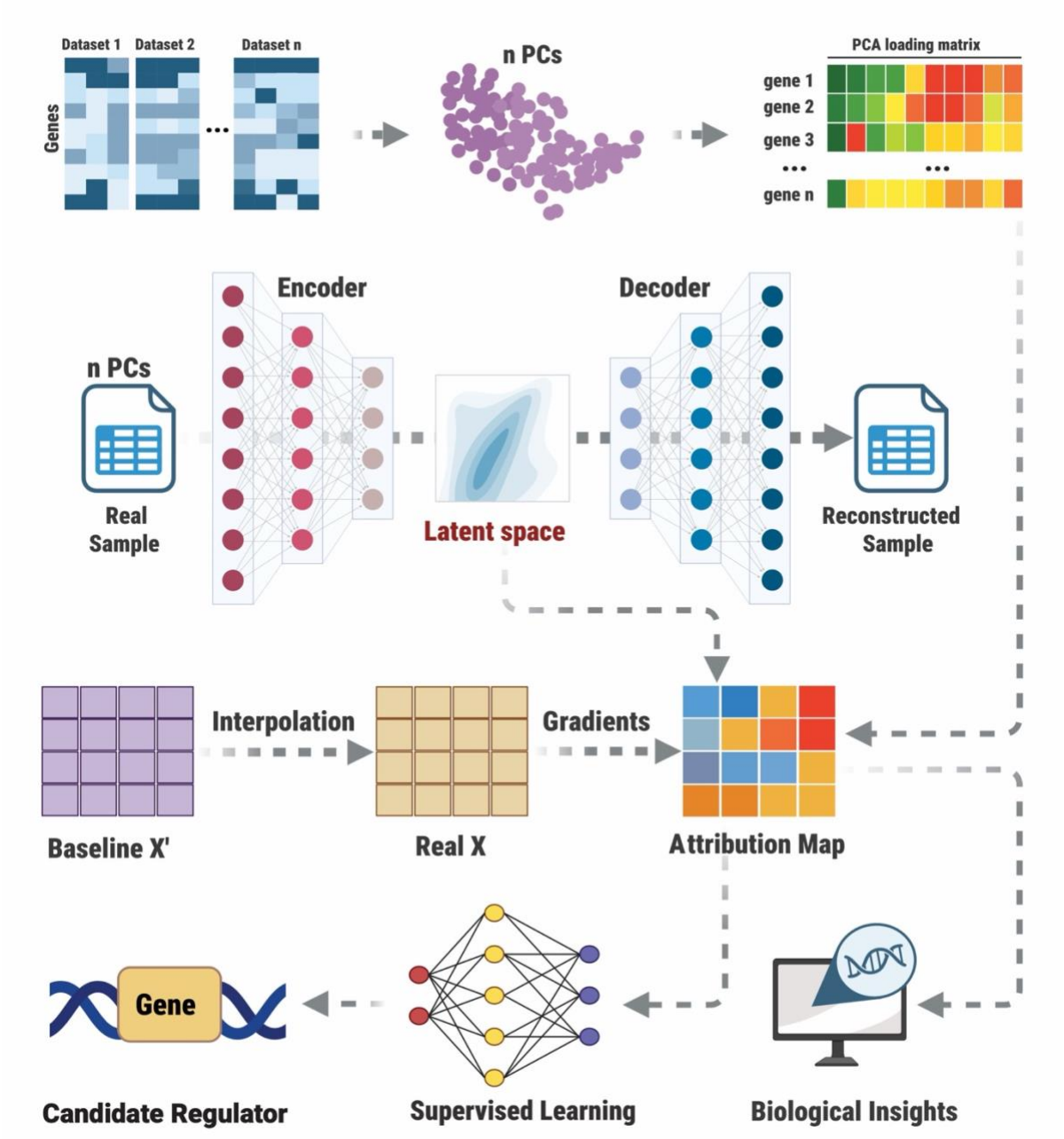


Figure 2.1: Workflow of the study pipeline. *PCA-transformed multi-dataset gene expression is encoded via VAE to latent space, followed by Integrated Gradients-based gene attribution and supervised learning to identify candidate regulators and extract biological insights of the latent spaces. [Figure generated using Adobe Illustrator v27.8.1].*

2.2 Datasets Retrieval

Publicly available gene-expression datasets of head and neck cancer generated using different platforms—including [HG-U133_Plus_2] Affymetrix Human Genome U133 Plus

2.0 Array, [HG-U133A] Affymetrix Human Genome U133A Array, [HG-U133B] Affymetrix Human Genome U133B Array, [HG-Focus] Affymetrix Human HG-Focus Target Array and Pathwork Diagnostics Pathchip (Homo sapiens)—were downloaded. A total of 26 datasets were parsed from the National Center for Biotechnology Information (NCBI) (https://www.ncbi.nlm.nih.gov/) Gene Expression Omnibus (GEO) (https://www.ncbi.nlm.nih.gov/geo/) database for head and neck cancer types, where a python library GEOparse v2.0.0 (https://github.com/guma44/GEOparse) was incorporated to extract the sequencing data with their phenotype data from the database server. All information about the datasets including sample size mentioned in **Table 2.1**.

Table 2.1 Expression Profiling Datasets for Head and Neck Cancer

GEO_Accession	Samples in series	Platform	Study_Type
GSE100942	10	GPL570 (Affymetrix HG-U133 Plus 2.0)	Expression profiling by array
GSE10300	44	GPL570 (Affymetrix HG-U133 Plus 2.0)	Expression profiling by array
GSE12630	276	GPL7280 (Pathwork Diagnostics Pathchip); GPL96 (Affymetrix HG-U133A)	Expression profiling by array
GSE17351	10	GPL570 (Affymetrix HG-U133 Plus 2.0)	Expression profiling by array
GSE2326	38	GPL97 (Affymetrix HG-U133B); GPL96 (Affymetrix HG-U133A)	Expression profiling by array
GSE27020	109	GPL96 (Affymetrix HG-U133A)	Expression profiling by array
GSE29330	18	GPL570 (Affymetrix HG-U133 Plus 2.0)	Expression profiling by array
GSE30784	229	GPL570 (Affymetrix HG-U133 Plus 2.0)	Expression profiling by array

GSE3292	36	GPL570 (Affymetrix HG-U133 Plus 2.0)	Expression profiling by array
GSE33810	3	GPL570 (Affymetrix HG-U133 Plus 2.0)	Expression profiling by array
GSE35603	78	GPL570 (Affymetrix HG-U133 Plus 2.0)	Expression profiling by array
GSE42363	14	GPL570 (Affymetrix HG-U133 Plus 2.0)	Expression profiling by array
GSE43580	150	GPL570 (Affymetrix HG-U133 Plus 2.0)	Expression profiling by array
GSE46517	121	GPL96 (Affymetrix HG-U133A)	Expression profiling by array
GSE4975	14	GPL96 (Affymetrix HG-U133A); GPL97 (Affymetrix HG-U133B); GPL570 (Affymetrix HG-U133 Plus 2.0)	Expression profiling by array
GSE51010	56	GPL570 (Affymetrix HG-U133 Plus 2.0); GPL201 (Affymetrix HG-Focus)	Expression profiling by array
GSE51021	28	GPL570 (Affymetrix HG-U133 Plus 2.0)	Expression profiling by array
GSE53355	44	GPL570 (Affymetrix HG-U133 Plus 2.0)	Expression profiling by array
GSE5364	341	GPL96 (Affymetrix HG-U133A)	Expression profiling by array
GSE56330	2	GPL570 (Affymetrix HG-U133 Plus 2.0)	Expression profiling by array

GSE60542	92	GPL570 (Affymetrix HG-U133 Plus 2.0)	Expression profiling by array
GSE6791	84	GPL570 (Affymetrix HG-U133 Plus 2.0)	Expression profiling by array
GSE74530	12	GPL570 (Affymetrix HG-U133 Plus 2.0)	Expression profiling by array
GSE76039	37	GPL570 (Affymetrix HG-U133 Plus 2.0)	Expression profiling by array
GSE78060	30	GPL570 (Affymetrix HG-U133 Plus 2.0)	Expression profiling by array
GSE84713	28	GPL570 (Affymetrix HG-U133 Plus 2.0)	Expression profiling by array

Extracted results according to the supplied ArrayExpress accession ids filtered out based on the treatment and condition of the samples. We got a total of 643 samples from all the datasets combined. Samples treated with radiation therapy, chemotherapy, targeted therapy, immunotherapy, hormonal therapy and drugs were excluded from the study manually.

2.3 Data Integration, Batch Effect Removal and Preprocessing

To amalgamate data from different platforms, a python data analysis library pandas v1.5.3 (McKinney 2011) was incorporated. Data imputation was conducted by missForest v0.9 (Stekhoven and Bühlmann 2012) package in R to avoid the NA values in the datasets. For concatenating multiple datasets from multiple platforms with different techniques, a batch effect correction method based on python library was applied on the integrated data to combat the platform specific biases. A function called “ComBat” from python library pyComBat v0.3.2 (Behdenna et al. 2023) was used to remove the technical biases that arose by the integration process. Expression data of merged dataset was log-transformed, Z-standardized on each gene to ensure that all features are on the same scale.

2.4 Training Deep Neural Network Models

2.4.1 Datasets Merging and Standardization

After manual selection and preprocessing, we had 643 cancer-positive samples, each containing 11020 genes—common in all datasets. Despite the high dimensional gene expression matrix, which was complex to interpret the samples with their condition, a principal component analysis was conducted with 500 PCs (n_components=500) while preserving all important data and variance among the samples. PCA was performed in R using the following packages: stats v4.2.3, factoextra v1.0.7 (Kassambara and Mundt 2020) for extraction and display of PCA results, and dplyr v1.1.4 (Hadley Wickham et al. 2020) for data manipulation.

2.4.2 Traditional Deep Learning Model

A probabilistic latent variable model was built on reduced PC data to learn a compact, non-linear delineation of the high-dimensional gene expression data. This is a type of neural network that contains an encoder and a decoder network with an entropy-limited latent mapping with *D* latent variables (here, $D \ll M$, where *M=500PC*, represents the number of features) in the middle. This process generates an embedding *Z*, which preserves the whole information of the input (*500PC*) into a lower dimensional space (Bro and Smilde 2014). Categorically, the encoder network, defined as $f_{\phi}: \mathrm{X} \rightarrow \mathrm{Z}$, maps from the input space $\mathrm{X} \in \mathbb{R}^{M}$ to latent embedding $\mathrm{Z} \in \mathbb{R}^{D}$. Similarly, the decoder network, defined as $g_{\varphi}: \mathrm{Z} \rightarrow \mathrm{X}$ maps the embedding Z back to input space. The main objective of the model is to minimize the anticipated squared Euclidean (L2) norm (Tian et al. 2017) between the input and its reconstruction:

$$\min_{\phi,\varphi} \mathbb{E} \left\| x - g_{\varphi}\left(f_{\phi}(x)\right) \right\|_{2}^{2} \qquad \text{... ... ... (i)}$$

Here in (i) equation, ϕ and φ are the parameters of the encoder and decoder, respectively, and $\hat{x} = g_{\varphi}\left(f_{\phi}(x)\right)$ represents the reconstructed input for every sample. Where, L2 loss denoted by $\| x - \hat{x} \|_{2}^{2}$, captures the total reconstruction error across all dimensions of the input. Overtly, this corresponds to:

$$(x_1 - \hat{x}_1)^2 + (x_2 - \hat{x}_2)^2 + \cdots + (x_n - \hat{x}_n)^2 \qquad \text{... ... ... (ii)}$$

2.4.3 Additional Sample Distribution

Unlike conventional approach, we used variational autoencoder (VAE), which encodes each sample as a probability distribution—captures uncertainty and biological variability inherent in gene expression profiles. Samples with 500 principal components (PCs) were used to construct the input matrix $X \in \mathbb{R}^{N \times M}$, where N is the number of samples and M is the number of features. This matrix was passed to an encoder f_θ, which outputs a mean vector $\mu_x \in \mathbb{R}^D$ and a variance vector $\sigma_x \in \mathbb{R}^D$:

$$\boldsymbol{f_\phi: x \to (\mu_x, \sigma_x), \quad Z \sim \mathcal{N}(\mu_x, \sigma_x) \quad \ldots \ldots \ldots \text{(iii)}}$$

A decoder g_φ reconstructs the input from the sampled latent vector Z. The model is trained to minimize the following loss:

$$\boldsymbol{\min_{\phi,\varphi} \mathbb{E} \parallel x - g_\varphi\left(f_\phi(x)\right) \parallel_2^2 + \mathrm{KL}[(\mu_x, \sigma_x), \mathcal{N}(0,1)] \quad \ldots \ldots \ldots \text{(iv)}}$$

The first term ensures accurate reconstruction, while the KL divergence regularizes the latent space by encouraging it to resemble a standard (Pan et al. 2020). After training, the learned latent variables Z were used for gene importance analysis using Integrated Gradients, followed by pathway enrichment.

2.5 Neural Network Design and Hyperparameter Optimization

2.5.1 Train Model with Adam Optimizer

VAE models were trained to unite the PCs from the head and neck cancer gene expression matrix as inputs. Three-layer encoder and decoder networks were designed as a mirror of each other. The model was trained in batches of 50 samples by using (Wang et al. 2022), with a learning rate of 0.0005, with weight initialized randomly using the Glorot uniform method.

2.5.2 Cross validate and Extract Best Latent Dimension

To determine the best fitted latent space as per my study, we deliberately selected a set of sizes: 5, 10, 25, 50, 75, and 100. This comprehensive selection was made to give our models a broad scope to capture a wide range of information from the datasets. Hyperparameter tuning was performed to fine-tune hyperparameters including the dropout rate and the number of neurons per layer using 5-fold cross-validation, guided by validation reconstruction error (Elgeldawi et al. 2021). We tested dropout values including 0, 0.2, 0.4,

and 0.6. For hidden layer configurations, we explored multiple settings such as (50, 5), (100, 25), (250, 50), (250, 100), and (300, 150), where the first and second values indicate the number of neurons in the first and second hidden layers, respectively. The model was implemented in Python using Keras v2.2.4 (Chollet 2015) and TensorFlow v1.12.0 (Filus and Domańska 2023).

2.6 Learning Robust Latent Representations

To find out the stable and fruitful biological representation of the data, VAE were trained with different random initializations and latent dimensionalities. For each latent size, training across multiple random seeds was repeated, resulting in a large collection of embeddings. To aggregate latent variables $\boldsymbol{Z} \in \mathbb{R}^d$ generated across multiple folds of different models, k-means clustering was applied to group (I) similar latent features together (Sinaga and Yang 2020). To obtain the final ensemble latent dimension $\boldsymbol{Z_{ensemble}} \in \mathbb{R}^L$, G-means clustering was implemented, resulting in a fixed latent size L=50, which was used across all samples for downstream analysis. The final latent embedding for each sample was constructed by averaging all latent variables within each cluster (Ri and Kim 2020).

2.7 Gene Attribution and Pathway Analysis

2.7.1 Sensitivity-Based Scoring (SBS) for Gene-to-Latent Attribution

To determine which gene contributed to what latent variables, a custom sensitivity-based scoring (SBS) approach was applied. SBS was first integrated into the method to calculate the importance of each PC for every latent variable. Then these attributions were scaled to gene level with the PC level weights, resulting in gene-level importance scores and by averaging we got global gene attributions for each latent.

2.7.2 Pathway Enrichment Analysis of Latent Variable-Associated Genes

To interpret the biological representation, top-ranked genes derived from every ensemble latent variable, we performed pathway enrichment analysis using the g:Profiler tool via the gprofiler2 v2.34 (Peterson et al. 2020) R package. Gene sets with the highest attribution scores were input into the gost() function, which maps genes to known functional categories including Gene Ontology (GO) terms (Biological Process, Molecular Function, Cellular Component), KEGG pathways, and Reactome pathways (Carbon et al. 2017; Jassal et al. 2020; Kanehisa et al. 2023). We used the default settings for the organism (*Homo sapiens*),

applied multiple testing correction via the Benjamini–Hochberg method (FDR < 0.05), and excluded electronic GO annotations to improve specificity (Ferreira and Zwinderman 2006). The results were visualized and ranked by adjusted p-values and term size to highlight the most enriched biological functions associated with each latent variable.

2.7.3 Gene Set Enrichment Analysis (GSEA)

To uncover the biological functions associated with each latent variable, we performed Gene Set Enrichment Analysis (GSEA) using pre-ranked gene lists derived from latent variable attributions (Balagopalan et al. 2009). The enrichment results were obtained using a standardized pipeline and summarized across all latent variables. Pathways with a false discovery rate (FDR) < 0.05 were considered statistically significant. We calculated the normalized enrichment score (NES) for each term-latent pair and constructed a matrix of NES values. To focus on the most variable biological patterns, we selected the top 50 pathways based on the highest variance across latent variables. These were visualized as a heatmap using the seaborn v0.11.5 (Waskom 2021)library in Python, highlighting pathway–latent associations that may represent underlying biological signals.

2.8 Supervised Deep Learning Model Training

2.8.1 Gene Selection and Data Collection

To identify candidate genes for HNSCC, we analyzed gene attribution scores generated by the Deep model across 50 latent variables. Based on this analysis, we selected 20 genes that consistently ranked among the top contributors across multiple latent dimensions. These candidate genes were validated using an independent dataset, which included both HNSCC and non-tumor control samples profiled on Illumina HiSeq 4000 and NovaSeq 6000 sequencing platforms.

2.8.2 Normalization and Batch Correction

To address potential batch effects and platform-specific variability, we applied gene-wise Z-score normalization within each batch. Following normalization, batch correction was carried out using the empirical Bayes method implemented in the pycombat v0.3.5. All data manipulation and preprocessing were performed using the pandas v2.2.1 and numpy v1.24.4 libraries, with additional support from scanpy v1.9.6 (Wolf et al. 2018) for annotation and matrix handling.

2.8.3 Model Development and Training

We developed and trained three types of deep learning models to classify samples into HNSCC or control groups based on the expression of the 20 selected genes. These models were implemented using TensorFlow 2.12.0 with the Keras backend. Hyperparameter tuning was conducted using the kerastuner library v1.3.5, and model performance was assessed through five-fold stratified cross-validation (Wazery et al. 2023). The optimal MLP architecture consisted of two hidden layers with 128 and 64 neurons respectively, each followed by ReLU activation and dropout layers with a rate of 0.2. A final sigmoid-activated output layer was used for binary classification (Tolstikhin et al. 2021). All models were trained using the Adam optimizer (Wang et al. 2022) (learning rate = 1e-4), binary cross-entropy loss, a batch size of 32, and early stopping based on validation loss with a patience of 10 epochs.

2.8.4 Evaluation and Visualization

Model performance was evaluated using two key metrics: area under the precision–recall curve (AUPRC) and area under the receiver operating characteristic curve (AUROC). Visualizations of model predictions, ROC curves, and PR curves were generated using matplotlib v3.8.0 and seaborn v0.13.2. All experiments were conducted in a Linux-based computing environment.

2.9 Differential Gene Expression analysis

Expression data were analyzed *using* DESeq2 v1.40.2 (Love et al. 2014). Low-expression entries were removed before normalization. Variance-stabilizing transformation was applied for visualization. Differential expression analysis was performed using negative binomial distribution, and significance was defined as adjusted p-value < 0.05 and absolute $\log_2$ fold change > 1. Volcano plots were generated using EnhancedVolcano v1.20.0 (Blighe et al. 2021).

Chapter Three

Result

3.1 Data Preprocessing and Quality Assessment

Highly expressive models such as deep neural networks tend to overfit when the sample size is small, we collected 26 available expression datasets from different platforms for human head and neck cancer. To remove the platform-specific biases, we preprocessed the datasets **(Figure 3.1A)**, manually excluded samples that did not satisfy the requirements, and finalized 643 samples for PCA, with 11020 genes common across all datasets. Standardized gene expression values were visualized using a boxplot **(Figure 3.1A)** among all the samples, showing consistent distribution across samples and confirming effective scalability. PCA was performed on the 643 samples expression to reduce the dimension of the features in 500 PCs

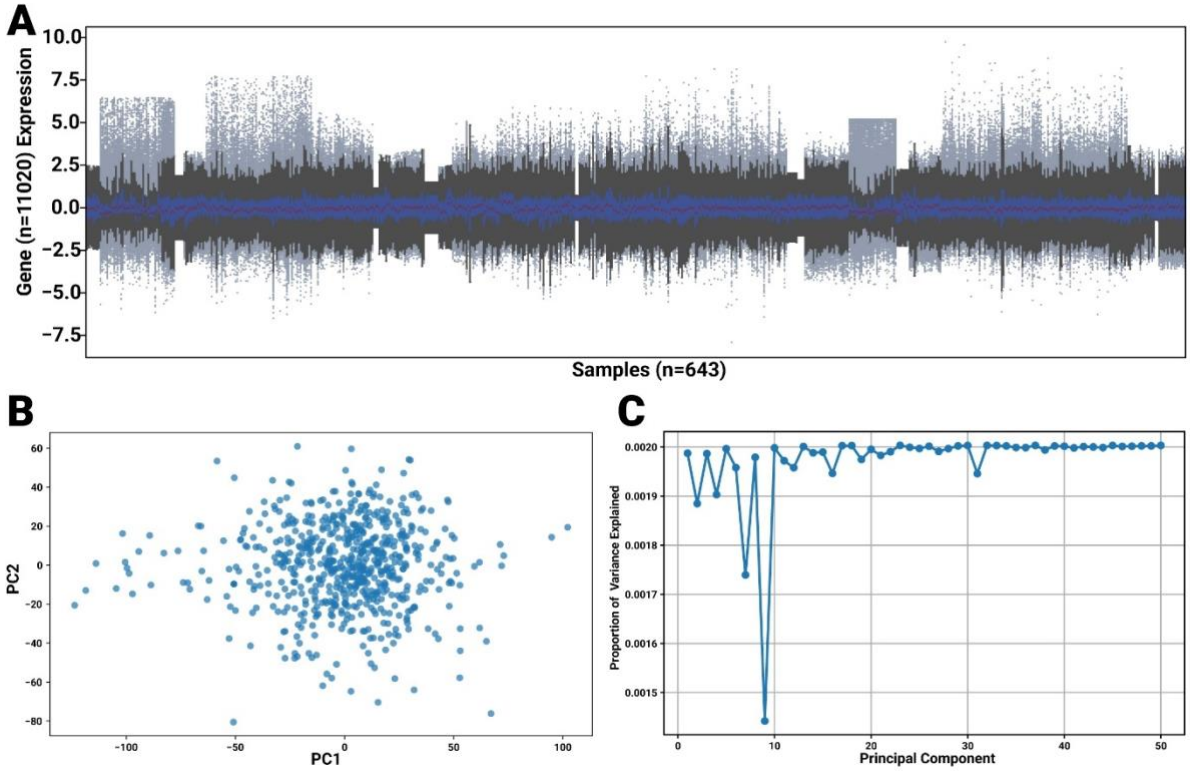


Figure 3.1: Preprocessing and PCA of gene expression data. ***(A)*** *Boxplot of standardized expression values for 11,020 genes across 643 finalized samples. Each box represents one sample, where dots represent outliers.* ***(B)*** *PCA scatterplot, containing the first two principal components for all samples; X axis containing PC1 and Y axis containing PC2* ***(C)*** *Scree plot showing the proportion of variance explained by the first 50 principal components. The variance contribution is uniformly low, supporting their use in downstream neural network training. [Figure generated using Python v3.12].*

for model training, where scatterplot **(Figure 3.1B)** showed no ostensible clustering or batch effect, indicating appropriateness for unsupervised modeling. The scree plot **(Figure 3.1C)** of the first 50 PCs shows uniformly low variance, confirmed that the components are evenly distributed. Other 450 PCs are similarly contained the same proportion of variance around 0.002. A minor drop in ratio in PC9 was observed, which likely reflects numerical or structural variance fluctuations other than biological interpretation.

3.2 Latent Space Extraction Using Deep Neural Network

Multiple models trained using the latent dimensions, including 5, 10, 25, 50, 75, and 100, and evaluated their ability to reconstruct the same sample using the parameters based on reconstruction error in both training and validation sets **(Figure 3.2A)**.

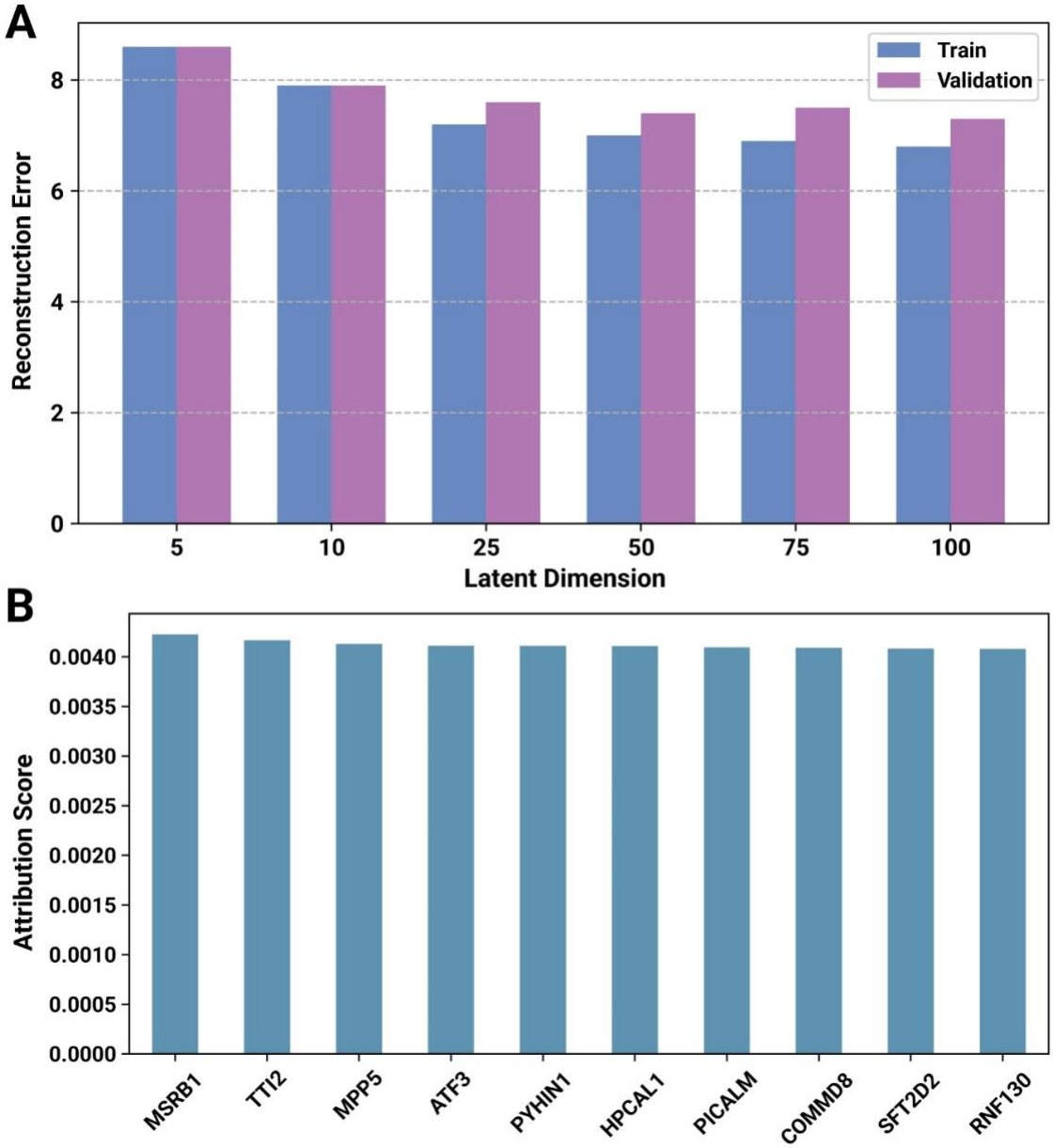


Figure 3.2: Model Performance and Gene Attribution. ***(A)*** *Barplot showing reconstruction error for both training and validation sets across different latent dimensions. X axis represents the latent nodes and Y axis showing the reconstruction error values.* ***(B)*** *Barplot showing the top 10 genes contributed to Latent Node 0, based on absolute Integrated Gradients (IG) scores from the ensemble attribution matrix. [Figure generated using Python v3.12].*

As the number of latent nodes increases, the reconstruction errors reduce as per the change, representing higher capacity of reconstruction. However, the improvement stops after 50 dimensions, which implies that higher nodes can increase the risk of overfitting the data as well as the complexity of the process. Therefore, we selected 50 nodes of latent to finalize the VAE models and got multiple folds of latent from all the models in each fold. This hyperparameter tuning helped us to reach the most relevant latent spaces, understand the core biology of head and neck cancer from the complex environment of the data.

Figure 3.2B, a sample representation of the top 10 genes in the first latent dimension, showing the strong connection with the latent node 0, ranked by their importance score. These genes, including MSRB1 (0.00416), TTI2 (0.00389), MPP5 (0.00358), ATF3 (0.00354), PYHIN1 (0.00349), HPCAL1 (0.00349), PICALM (0.00342), COMMD8 (0.0033), SFT2D2 (0.00325), RNF130 (0.00320), are the primary contributors to the representation/signal captured by this latent space. Top 10 contributors to the representation from all 50 latents mentioned in **Appendix I**.

3.3 Latent Variables Capture Distinct Gene Programs and Biological Pathways

To characterize the biological meaning of the latent space learned by the VAE model, we analyzed gene-level attributions using Integrated Gradients. We computed mean attribution scores for each gene across all 50 latent variables (latent nodes) and selected the top 20 genes with the highest overall contributions **(Figure 3.3A)**. These included genes such as DDX43, FABP4, RAP1GAP2, KCNK5, XIST, ZNF839, CTH, ERC2, and PDK3, among others. Mean attribution scores across latents ranged from 0.0035 to 0.0055, with FABP4 and CTH contributing strongly to Latent 24 and 25, and ERC2 and ZNF839 dominating Latent 28, indicating distinct gene modules regulating each latent.

Hierarchical clustering of latent variables based on gene attribution profiles revealed modular structures, where sets of genes co-regulated subsets of latent nodes. For instance,

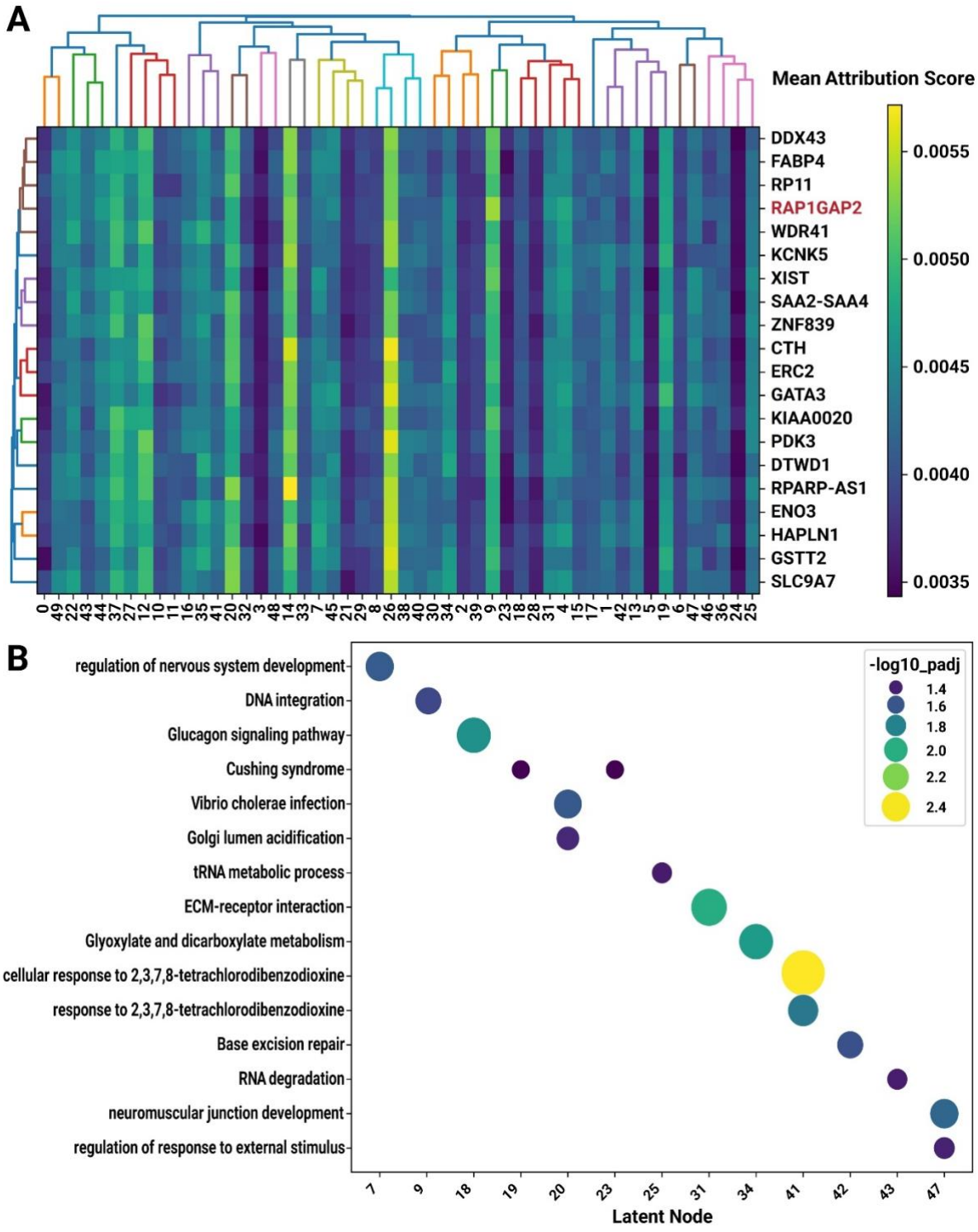


Figure 3.3: Interpretation of VAE latent variables through gene attribution and pathway enrichment. ***(A)*** *Heatmap showing the mean Integrated Gradients attribution scores of the top 20 genes across all 50 latent variables. Both rows (genes) and columns (latents) were hierarchically clustered, revealing modular structures among gene-latent relationships.* ***(B)*** *Dot plot summarizing the most significantly enriched biological pathways for selected latent variables. Each dot represents a latent-pathway pair, with dot*

size and color corresponding to the enrichment significance ($-\log_{10}$ padj). [Figure generated using Python v3.12].

Latents 24, 25, and 28 clustered closely and shared top-contributing genes involved in lipid metabolism and oxidative stress response, such as FABP4, CTH, and SAA2-SAA4.

Figure 3.3B illustrates the g: Profiler enrichment analysis of top-ranking genes from individual latent variables. Each dot represents a significantly enriched biological process, mapped to its corresponding latent node. Several latent variables were linked to distinct and functionally relevant pathways. For example, Latent 9 showed strong enrichment for DNA integration, suggesting potential involvement in genomic stability or viral interaction processes. Latent 20 was enriched for Golgi lumen acidification and Golgi-associated signaling, indicating a role in intracellular trafficking and post-translational modification. Latent 5 was associated with regulation of nervous system development, while Latent 33 was enriched for ECM-receptor interaction, pointing toward microenvironmental and adhesion-related mechanisms. Pathways related to RNA degradation (Latent 39), base excision repair (Latent 34), and neuromuscular junction development (Latent 45) were also identified, reflecting the biological diversity embedded within the latent dimensions. A complete table of enriched pathways, including adjusted p-values, enrichment scores, and associated gene sets for all 50 latent, is provided in **Appendix II**.

3.4 Functional Characterization of Latent Variables via GSEA

To further evaluate the functional relevance of the latent space, we performed Gene Set Enrichment Analysis (GSEA) using the ranked gene attributions for each of the 50 latent variables and visualized the results in a pathway–latent heatmap **(Figure 3.4A)**. The heatmap displays the Normalized Enrichment Scores (NES) across a curated panel of KEGG pathways, capturing the direction and magnitude of enrichment. Red tones indicate positive enrichment (NES > 0), whereas blue tones indicate negative enrichment (NES < 0).

Several latent variables were significantly enriched for known cancer-related and immune-related pathways. Latent 6 and Latent 21 were positively enriched for Ribosome and Oxidative Phosphorylation, processes often upregulated in proliferative tumor cells. Latent 15 and Latent 24 showed strong positive enrichment in immune pathways such as JAK-STAT signaling, Cytokine–cytokine receptor interaction, and Antigen processing and presentation. Latent 36 and Latent 48 were associated with Mismatch repair, Fanconi

anemia, and Cell cycle, indicating potential links to genomic instability. Negative enrichment was observed for several inflammation-related pathways (e.g., Inflammatory bowel disease, Primary immunodeficiency, NF-kappa B signaling), particularly in Latents 3, 9, and 18. Other Results of GSEA mentioned in **Appendix III.**

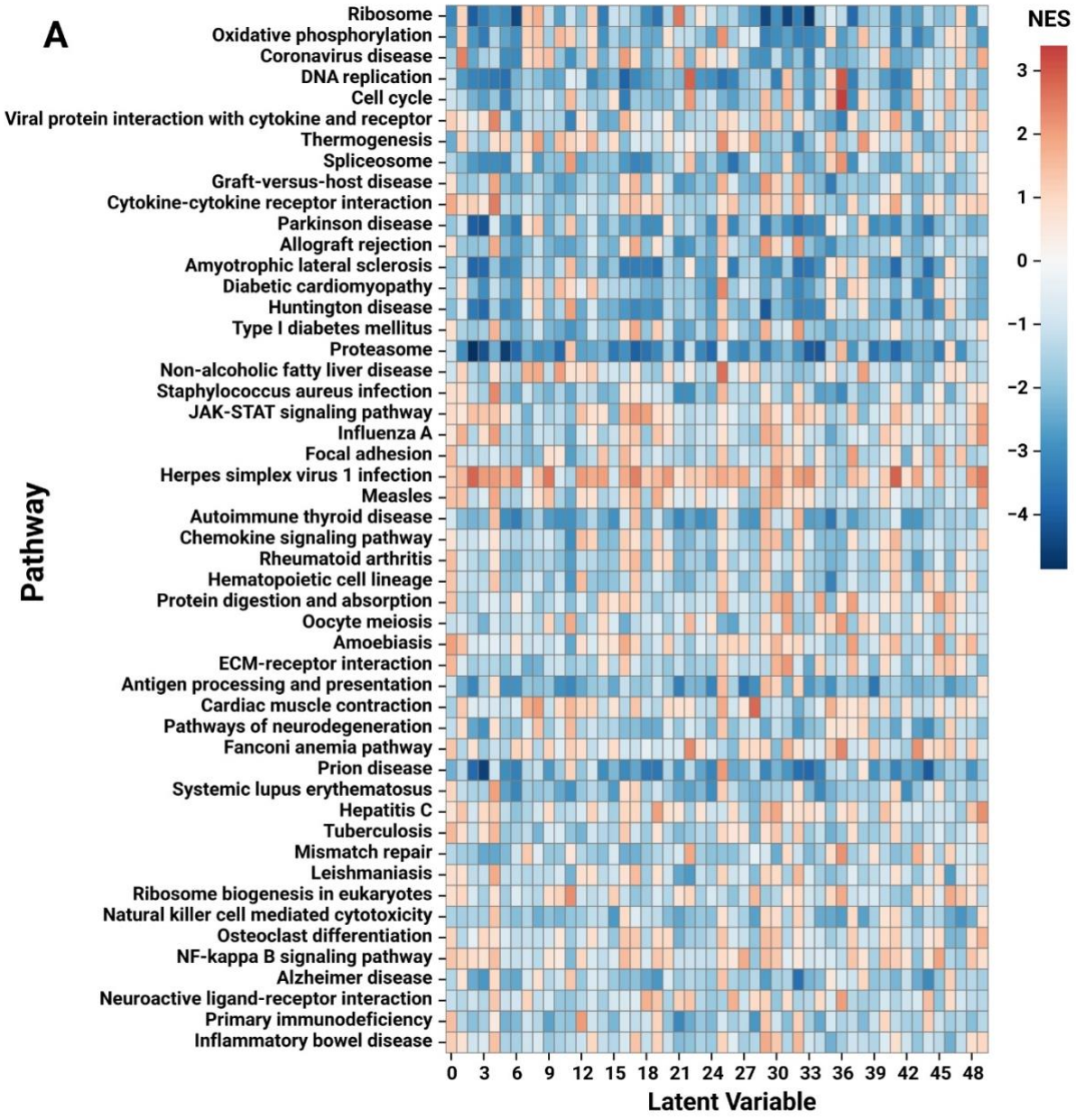


Figure 3.4: Pathway enrichment heatmap of VAE latent variables using GSEA. *Heatmap shows NES for pathways enriched across 50 latent variables. Each row represents a pathway and each column a latent node. Red shades indicate positive enrichment (NES > 0) and blue shades indicate negative (NES < 0). [Figure generated using Python v3.12].*

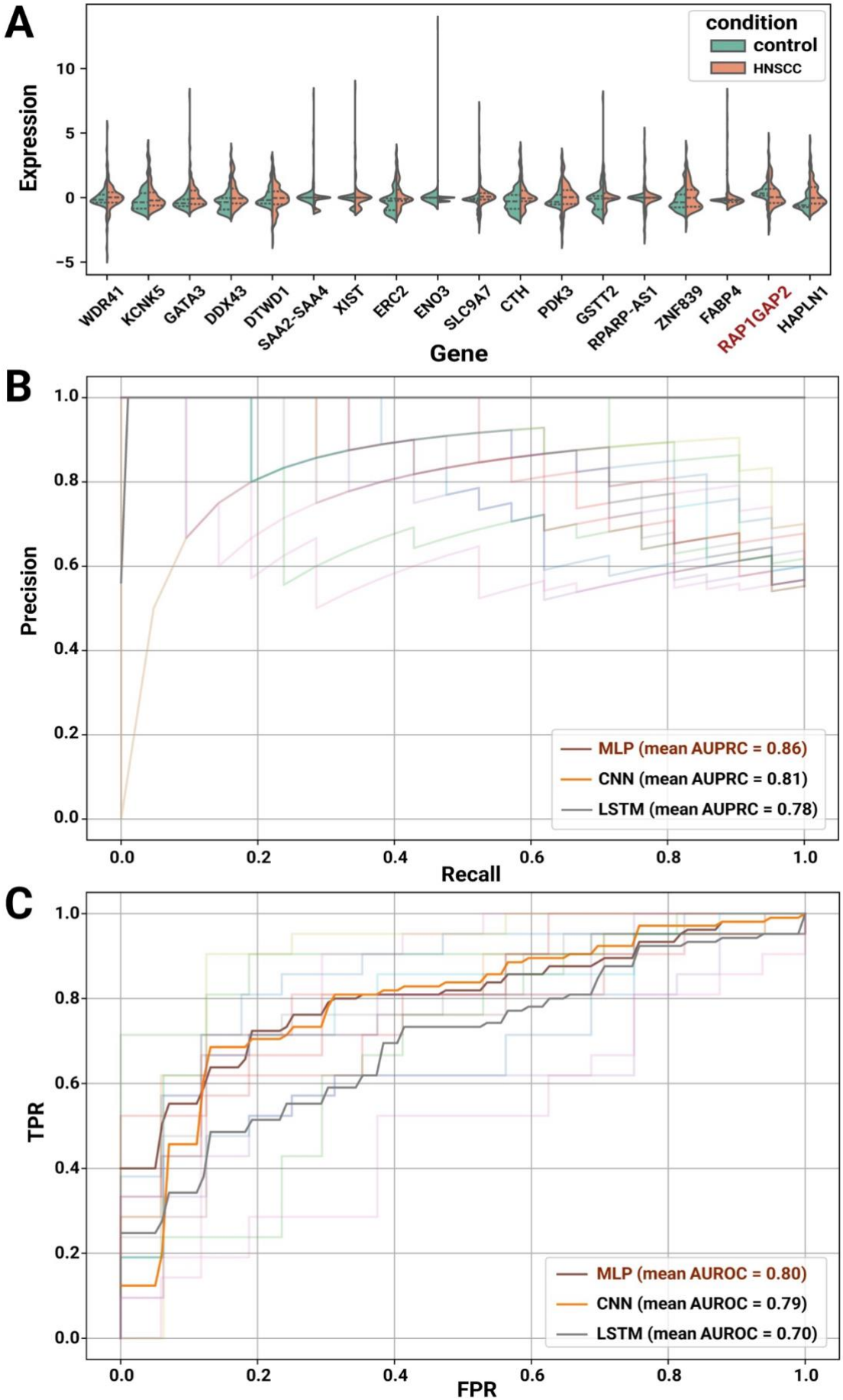

A
condition
control
HNSCC
Expression
10
5
0
−5
WDR41
KCNK5
GATA3
DDX43
DTWD1
SAA2-SAA4
XIST
ERC2
ENO3
SLC9A7
CTH
PDK3
GSTT2
RPARP-AS1
ZNF839
FABP4
RAP1GAP2
HAPLN1
Gene
B
Precision
1.0
0.8
0.6
0.4
0.2
0.0
MLP (mean AUPRC = 0.86)
CNN (mean AUPRC = 0.81)
LSTM (mean AUPRC = 0.78)
0.0
0.2
0.4
0.6
0.8
1.0
Recall
C
TPR
MLP (mean AUROC = 0.80)
CNN (mean AUROC = 0.79)
LSTM (mean AUROC = 0.70)
FPR

Figure 3.5: Identification of candidate genes and classification performance in HNSCC. ***(A)*** *Violin plots showing the expression distributions of 20 consensus genes, derived from VAE latent space attribution scores, across control and HNSCC samples in an external high-throughput RNA-seq dataset.* ***(B)*** *Precision–Recall (PR) curves comparing three supervised deep learning models trained on the expression profiles of the 20 genes.* ***(C)*** *Receiver operating characteristic (ROC) curves for the same models. [Figure generated using Python v3.12].*

3.5 Deep Learning-Based Classification of Candidate Genes in HNSCC

To visualize the expression profiles of the 20 candidate genes across control and HNSCC samples, we generated violin plots **(Figure 3.5A)** and boxplots in **Appendix IV**. Most genes showed overlapping expression distributions between the two groups. RAP1GAP2 did not show a large expression difference between HNSCC and control samples, consistent with its failure to meet the fold-change threshold in the differential expression analysis (Figure 3.7C), so its value for classification does not rest on a large shift in average expression. Genes such as XIST and ERC2 displayed more variable patterns, hinting at subtype-specific or microenvironmental influences. We then assessed the ability of the 20-gene panel to classify HNSCC using supervised deep learning models. As shown in the performance plots (Figure 3.5B & C), the MLP model consistently outperformed CNN and LSTM across all evaluation folds. The MLP achieved a mean AUPRC of 0.86 and mean AUROC of 0.80, followed by the CNN with an AUPRC of 0.81 and AUROC of 0.79, and the LSTM with an AUPRC of 0.78 and AUROC of 0.70.

These results indicate that the MLP model is best suited for classifying HNSCC based on the selected latent-informed gene set. The consistently high AUPRC and AUROC suggest that the VAE-derived genes, particularly RAP1GAP2, PDK3, and FABP4, may serve as effective candidate markers or classifiers for HNSCC in high-throughput transcriptomic data **(Table 3.1), (Appendix V)**.

3.6 RAP1GAP2 Emerges as the Most Predictive Gene in Single-Feature Classification Models

To identify the most predictive gene within the consensus panel, we trained single-feature models for each of the 20 genes and computed their individual feature importances using the supervised MLP model described previously. The resulting importance scores are visualized in **Figure 3.6A**, where RAP1GAP2 ranked as the most informative gene,

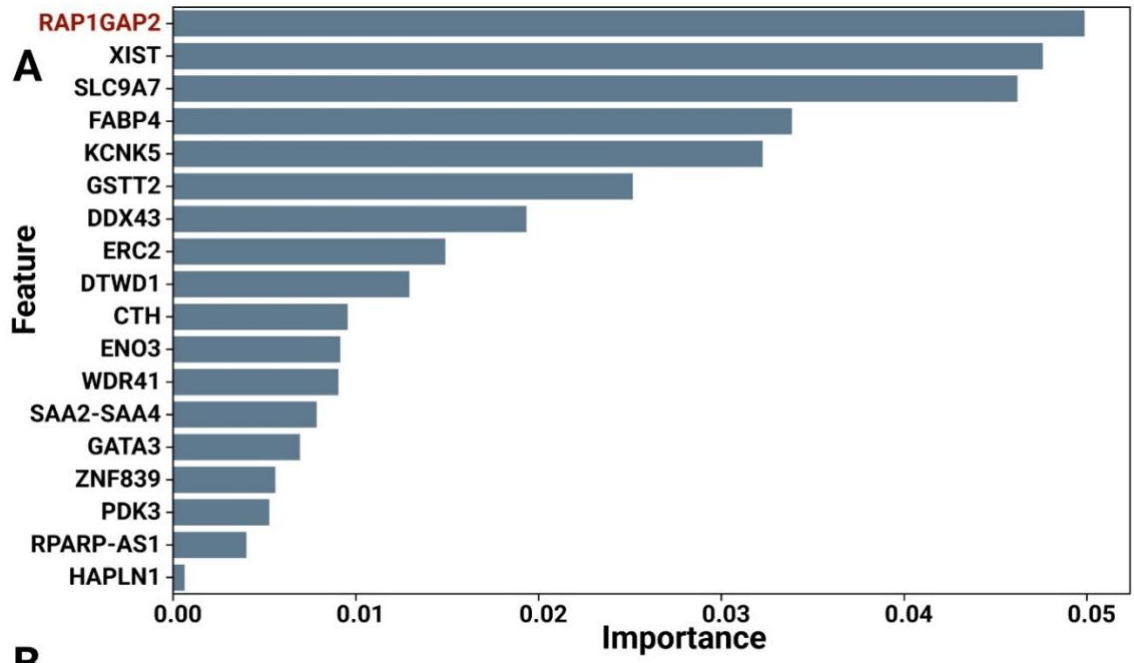
followed closely by XIST, SLC9A7, and FABP4. This suggests that RAP1GAP2 holds strong discriminative power for separating HNSCC from control samples, reinforcing its prominence in both latent attribution analysis and expression profiling.

To validate its predictive strength, we constructed a single-gene MLP classifier using only the expression values of RAP1GAP2. The resulting Precision–Recall curve, shown in **Figure 3.6B**, achieved a mean AUPRC of 0.769, indicating robust classification performance using this gene alone. This further supports the hypothesis that RAP1GAP2 may serve as a candidate biomarker of HNSCC and warrants further experimental validation.

Table 3.1 Performance metrics for single-gene classification models

Gene	AUROC	AUPRC	Accuracy	F1	Precision	Recall
WDR41	0.640	0.650	0.556	0.711	0.560	0.971
KCNK5	0.540	0.560	0.524	0.686	0.545	0.924
GATA3	0.590	0.580	0.620	0.667	0.657	0.676
DDX43	0.550	0.570	0.513	0.629	0.550	0.733
DTWD1	0.650	0.640	0.535	0.679	0.554	0.876
XIST	0.594	0.708	0.540	0.688	0.556	0.905
SAA2-SAA4	0.557	0.621	0.556	0.709	0.561	0.962
ERC2	0.550	0.560	0.610	0.709	0.610	0.848
ENO3	0.610	0.590	0.567	0.722	0.565	1.000
SLC9A7	0.710	0.710	0.594	0.689	0.604	0.800
CTH	0.590	0.590	0.604	0.711	0.603	0.867
PDK3	0.570	0.600	0.567	0.675	0.583	0.800
GSTT2	0.643	0.664	0.642	0.735	0.628	0.886

RPARP-AS1	0.528	0.619	0.540	0.699	0.552	0.952
ZNF839	0.550	0.590	0.556	0.711	0.560	0.971
FABP4	0.520	0.530	0.535	0.695	0.550	0.943
RAP1GAP2	0.710	0.769	0.730	0.760	0.700	0.940
HAPLN1	0.606	0.676	0.615	0.692	0.628	0.771



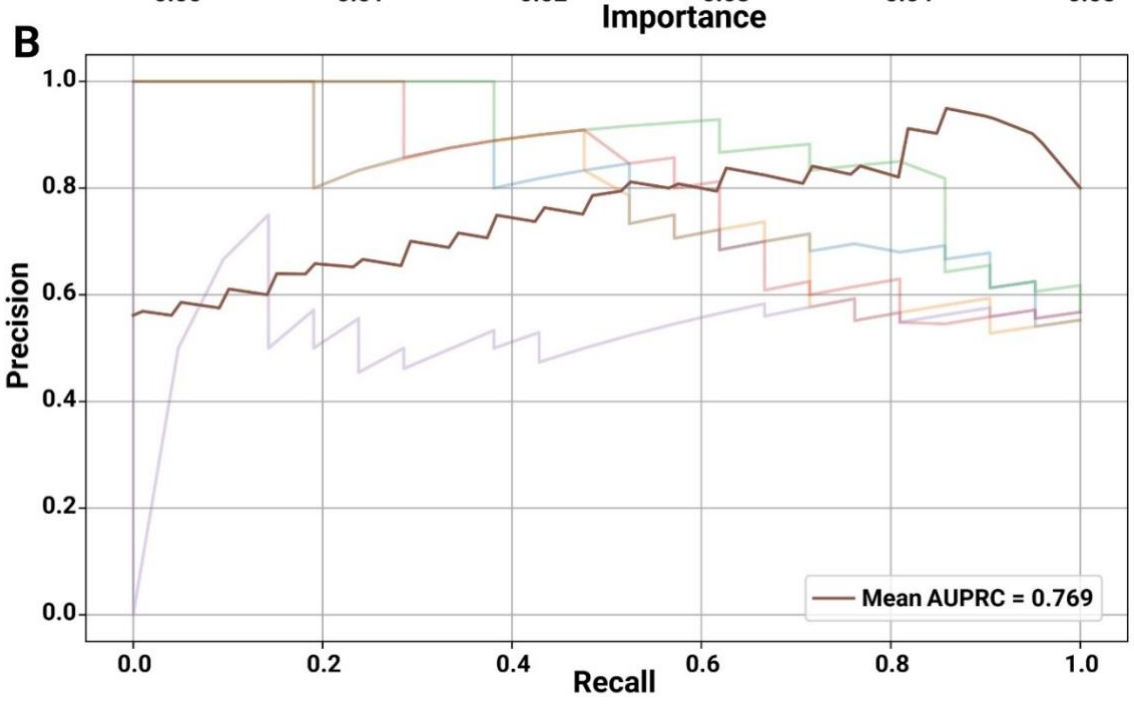


Figure 3.6: RAP1GAP2 identified as the top predictive gene for HNSCC classification. ***(A)*** *Feature importance scores for each of the 20 genes in the supervised MLP model. RAP1GAP2 ranked highest, suggesting its dominant role in classification.* ***(B)*** *Precision–Recall curve for the single-gene classifier trained exclusively on RAP1GAP2 expression. The model achieved a mean AUPRC of 0.769, indicating strong predictive capacity from this gene alone. [Figure generated using Python v3.12].*

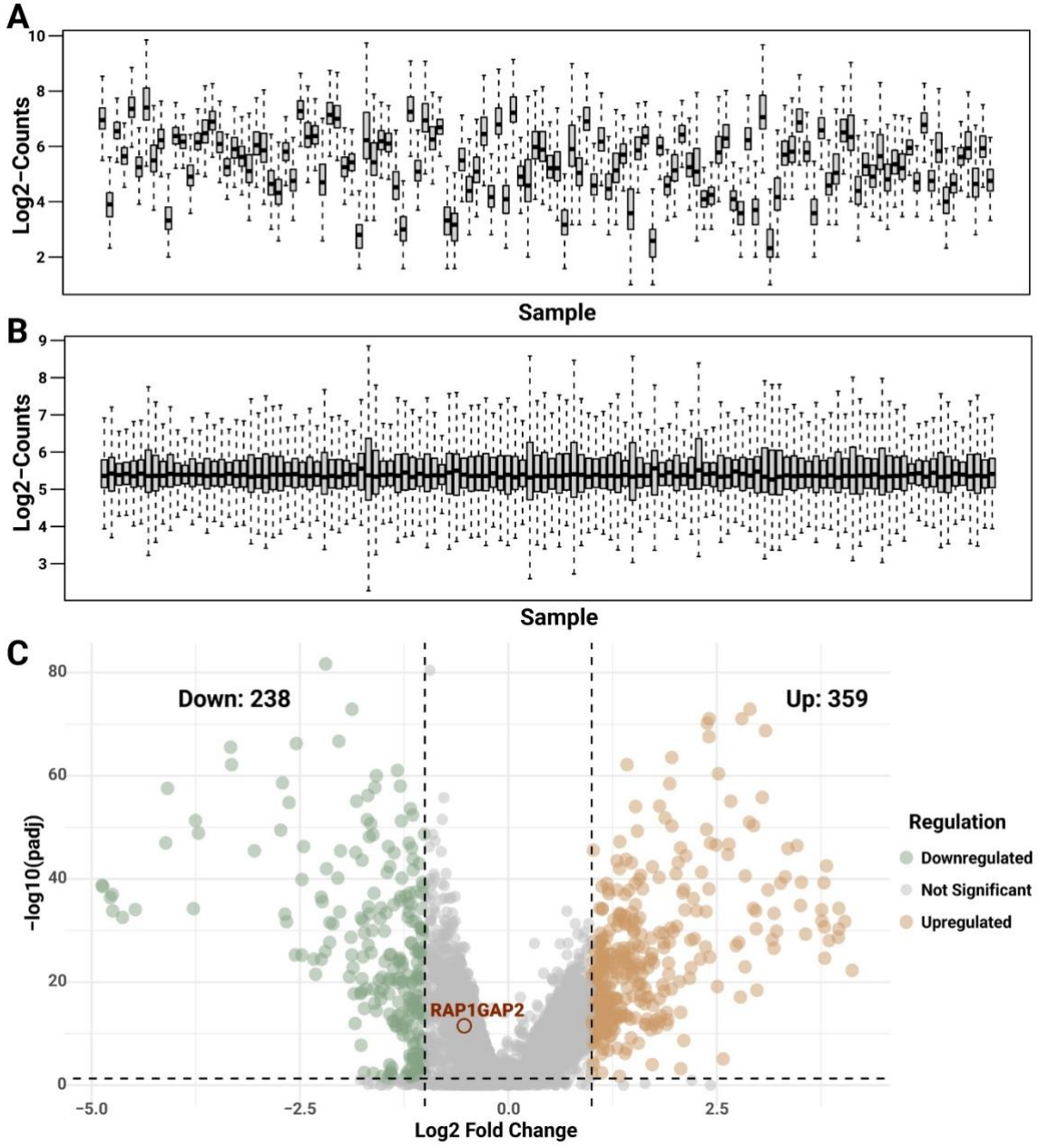


Figure 3.7: Identification of RAP1GAP2 as a latent candidate regulator despite non-significance in differential expression analysis. ***(A)*** *Raw gene expression across samples before normalization.* ***(B)*** *Normalized expression profiles of all samples.* ***(C)*** *Volcano plot*

of differential gene expression analysis: upregulated, downregulated, and non-significant genes are shown. RAP1GAP2, highlighted in red, was not significantly differentially expressed but was identified as a top contributor across all latent variables and showed the highest classification ability in the deep learning model, supporting its status as a latent candidate regulator in HNSCC. [Figure generated using R v4.3.2 with RStudio v2023.09.1].

3.7 RAP1GAP2 Emerges as a Latent Candidate Regulator Despite Non-Significance in Differential Expression Analysis

Figure 3.7A & B show the gene expression distributions of the RNA-seq datasets before and after normalization, respectively. **Figure 3.7A** illustrates the raw, unnormalized transcript counts, highlighting variability across samples.

In contrast, **Figure 3.7B** demonstrates the effect of DEseq2 normalization, resulting in more comparable and standardized expression profiles across all samples, ensuring the reliability of downstream analyses.

However, differential gene expression (DGE) analysis failed to identify RAP1GAP2 as significant in LFC values. As shown in **Figure 3.7C**, RAP1GAP2 resides within the "not significant" region of the volcano plot, indicating that it was not differentially expressed based on standard thresholds (log2 fold change and FDR-adjusted p-value).

Chapter Four

Discussion

4.1 Discussion

This study employed a deep learning framework to reveal novel molecular patterns and latent candidate regulators overlooked by traditional methods, utilizing transcriptome data from head and neck cancer. We successfully reduced the data to 50 low-dimensional, biologically interpretable latent variables by training a variational autoencoder on high-dimensional gene expression matrices. By maintaining essential variation among samples, these latent traits enabled downstream modeling to reveal functional insights. A 50-dimensional embedding yielded the optimal balance between biological richness and training error when evaluating the reconstruction quality of the VAE across various latent dimensionalities **(Figure 3.1)**. The model's capacity to delineate the underlying illness structure was emphasized by the UMAP display of the acquired embeddings, which distinctly segregated the head and neck cancer subgroups **(Figure 3.2)**.

Integrated Gradients were employed to quantify the contribution of each gene to each latent dimension, thereby enhancing the understanding of the biological relevance of these representations. The analysis revealed the presence of high-attribution gene sets that were not restricted to individual dimensions but were also enriched for key biological pathways, as identified through Gene Ontology and KEGG annotations **(Figure 3.4)**. Several latent variables were associated with biological processes such as cell adhesion, immune signaling, and extracellular matrix remodeling—mechanisms commonly implicated in tumor progression. In many cases, high-contribution genes appeared recurrently across multiple latent dimensions, indicating that shared biological programs may be embedded within distinct transcriptomic patterns. These results confirmed that the latent space captured by the model reflects physiologically meaningful signals and provided justification for further examination of genes contributing across dimensions.

This study aimed to investigate the molecular intricacies of HNSCC via a deep learning analytical framework that transcends the limitations of conventional differential gene expression techniques. Utilizing a variational autoencoder (VAE) grounded on a neural network framework, and subsequently applying gene attribution through integrated gradients, we identified 50 latent dimensions that encapsulate compressed, physiologically significant transcriptome patterns. The latent dimensions were enriched for specific gene programs and biological pathways **(Figure 3.3, 3.4)**, uncovering concealed aspects of HNSCC biology not addressed by conventional linear methods. RAP1GAP2 appeared as a notably consistent and discriminative component among the genes contributing to these

latent traits **(Figure 3.6)**. Despite its robust latent-space attribution and efficacy as a single-gene classifier (AUPRC ≈ 0.77), RAP1GAP2 was not deemed significant in LFC in the differential expression study **(Figure 3.7C)**. The disparity between statistical insignificance and biological significance underscores the fundamental value of our approach—deep generative models can reveal non-linear molecular determinants that traditional methods may overlook.

Our results align with and contribute to the existing knowledge in the subject. Researchers have long recognized that the Ras-related GTPase Rap1 and its regulators influence the adhesion and motility of cancer cells (Zhang et al. 2017). Active Rap1 signaling has been demonstrated to enhance the invasiveness of head and neck malignancies by inducing the production of β-catenin and MMP7 (Zhang et al. 2017). Conversely, the Rap1 inactivator RAP1GAP, a paralog of RAP1GAP2, inhibits Rap1–ERK signaling and tumor proliferation in HNSCC models derived from the oropharynx (Zhang et al. 2006). Our identification of RAP1GAP2 enhances this paradigm while introducing a novel element. RAP1GAP2 functions as a pro-invasion factor, whereas Rap1GAP broadly inhibits HNSCC growth (Zhang et al. 2006). Upon examining the entirety of the situation, this seeming contradiction becomes comprehensible: Rap1 regulators frequently exert disparate effects on various cell types (Zhang et al. 2017). Research indicates that Rap1GAP often inhibits invasion in various malignancies; but, in certain instances, elevated levels of Rap1GAP may enhance cellular invasiveness (Zhang et al. 2017). Our findings indicate that HNSCC exemplifies a scenario in which RAP1GAP2, functioning in a specific cellular region, promotes cancer proliferation. This constitutes a novel discovery, as RAP1GAP2 has not been previously examined in HNSCC; it was a latent candidate regulator identified by our latent-space profiling.

We identified additional latent candidate genes, including PDK3 and FABP4, that corroborate the biological validity of our methodology. PDK3 (pyruvate dehydrogenase kinase 3) is a recognized mediator of the Warburg effect and is increased in hypoxic malignancies, resulting in metabolic reprogramming and aggressive behavior (Lu et al. 2011). FABP4 (fatty acid–binding protein 4) facilitates tumor metastasis and treatment resistance by accelerating lipid transport and signaling in cancer cells (Sun and Zhao 2022). Our model appears to have encapsulated significant characteristics of cancer, such as metabolic plasticity and microenvironmental adaptation, alongside the Rap1 signaling axis. The presence of PDK3 and FABP4 among our principal latent genes demonstrates this.

The alignment of our data-driven discoveries with established cancer pathways corroborates the outcomes of our study. We have identified a novel candidate regulator (RAP1GAP2) and an accompanying array of genes implicated in HNSCC invasion and demonstrated that deep neural profiling can uncover biologically significant targets overlooked by conventional techniques.

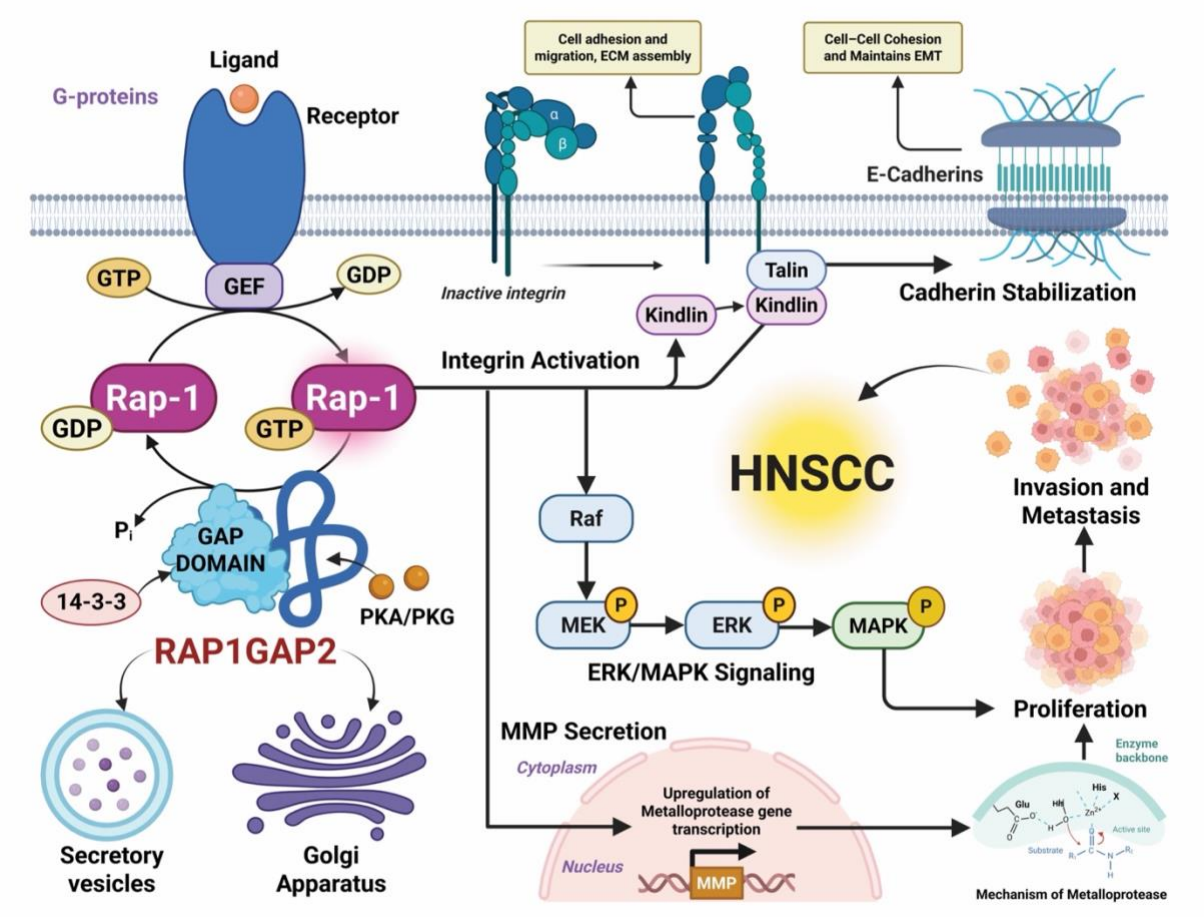


Figure 4.1: Schematic model illustrates the proposed role of RAP1GAP2 in promoting invasion and metastasis in HNSCC. *[Figure generated using Adobe Illustrator v27.8.1].*

RAP1GAP2 is a GTPase-activating protein (GAP) for Rap1 (Johansen et al. 2023). It changes active GTP-bound Rap1 into an inactive GDP-bound state, which changes how cells stick together and send signals. Active Rap1 stabilizes integrins and E-cadherins, which helps cells stick together and keeps epithelial cells looking like epithelial cells (Price et al. 2004). RAP1GAP2 stops Rap1 from working, which breaks up these stable interactions and makes cells lose their ability to stick together. This is necessary for tumor cells to start moving and invading.

RAP1GAP2 inactivates Rap1, which not only stops adhesion but also stops Rap1 from stopping Ras–MAPK/ERK signaling. This makes the ERK pathway more active (Zhang et al. 2017). ERK signaling helps cells grow, move, and turn on invasive genes, such as matrix metalloproteinases (MMPs). This makes tumors even more aggressive (Mitra et al. 2008).

RAP1GAP2 also affects how tumors invade by changing how vesicles move around. It works with the synaptotagmin-like protein 1 (Slp1) and Rab27 complex to control secretory vesicles that come from the Golgi apparatus (Neumüller et al. 2009; Li et al. 2018). This interaction leads to the release of enzymes that break down the matrix, like MMP-2 and MMP-9, into the extracellular space. This makes it easier for tissues to break down and makes them more invasive (Mitra et al. 2008; Beroun et al. 2019).

So, RAP1GAP2 controls a coordinated, multi-dimensional invasion strategy: it weakens cellular adhesion, turns on pro-invasive ERK/MAPK signaling, and boosts Golgi's ability to secrete proteases (Guo et al. 2020). This integrated mechanism shows how RAP1GAP2 can help metastasis even though it acts as a Rap1 inhibitor. Future experiments can test whether changing the expression of RAP1GAP2 affects the strength of cell adhesion, the levels of ERK activation, and the release of invasive factors. This would confirm its many roles in the progression of HNSCC. Notably, this latent contribution of RAP1GAP2 is captured by our model despite its lack of prominence in linear analysis, indicating that its contribution, while subtle at the expression level, is indeed biologically significant. Overall, the identification of RAP1GAP2 through latent-space analysis—supported by attribution, classifier performance, and mechanistic plausibility—highlights both the biological relevance of this gene and the power of our approach to reveal novel candidate regulators in HNSCC.

4.2 Limitations of the Study

Based on integrative analyses of transcriptomic data, our study identifies RAP1GAP2 as a promising computationally predicted candidate gene in HNSCC. To preserve a fair interpretation, a few restrictions must be noted.

First off, we didn't carry out functional tests to confirm RAP1GAP2's involvement in cellular functions like invasion and metastasis. Therefore, our results are still correlative, and there is no proof that RAP1GAP2 causes tumor behavior. Second, even with batch effect correction and gene harmonization, heterogeneity is introduced because we used retrospective integration of several public datasets from various platforms and clinical

subgroups. Variations in tumor subsite, treatment history, and HPV status could affect the latent features that are extracted. Third, some candidate genes (such as RAP1GAP2) showed only slight expression changes and might contribute to false positives because our machine learning pipeline gave predictive power precedence over statistical significance. Although this risk was reduced by cross-validation, biological significance still needs to be ascertained through experimentation. Furthermore, we were unable to assess the prognostic significance of the identified candidate genes due to the restricted availability of comprehensive clinical endpoints, such as survival and metastasis data. Lastly, we only looked at the mRNA level, leaving out other regulatory mechanisms that could have a significant impact on RAP1GAP2's function, like mutations, epigenetic changes, and post-translational events. All of these drawbacks highlight the necessity of additional research that includes multi-omic integration and experimental validation in order to completely clarify the biological and therapeutic significance of our findings.

4.3 Future Directions

Our results provide several avenues for additional research to confirm and broaden the biological significance of RAP1GAP2 in HNSCC. First and foremost, functional validation is essential. RAP1GAP2's function would be directly tested by knocking down or overexpressing it in HNSCC cell lines and evaluating cell invasion, Rap1-GTP activity, and downstream signaling (such as ERK/MAPK and MMP secretion). Its pro-metastatic role may be further supported by in vivo models. RAP1GAP2's value as a biomarker may be defined clinically by assessing its expression in larger patient cohorts or tissue arrays, which may show associations with tumor stage, metastasis, HPV status, or prognosis.

From a therapeutic standpoint, RAP1GAP2's downstream pathways, like MAPK signaling or Rab27-mediated secretion, provide actionable targets, even though directly targeting it may be challenging. Inhibitors of these effectors in RAP1GAP2-high models may be investigated in future research. To find cross-layer or context-specific candidate regulators, our deep profiling framework can be methodologically extended to other cancers or combined with proteomic and epigenetic data. New patterns may be found by applying the pipeline to HPV-stratified HNSCC datasets.

Lastly, more research is necessary to fully understand the network of interactions between latent candidate genes such as RAP1GAP2, PDK3, and FABP4. Studies on gene perturbation and systems biology may shed light on whether these genes are linked by

common regulators (like hypoxia) and provide combinatorial intervention points. Collectively, these avenues will enhance our comprehension of the function of RAP1GAP2 and facilitate the realization of our computational approach's translational potential.

Chapter Five

Conclusion

5. Conclusion

In summary, this study demonstrates that new cancer-causing factors can be identified by combining deep learning with high-dimensional transcriptome data. We discovered that RAP1GAP2, a gene that is rarely observed to exhibit differential expression, might play a secret role in regulating the invasion of other tissues by HNSCC. This new knowledge links biological mechanisms to data-driven modeling. It implies that these cancers become more aggressive due to dysregulation of Rap1 signaling (via RAP1GAP2), as well as modifications in metabolism and secretion. Our discussion demonstrates how this finding aligns with our current understanding of cancer pathways and provides a fresh perspective on and method for testing metastasis. Identifying RAP1GAP2 as a candidate regulator is a step toward improved prognostic tools and customized treatments for HNSCC. Ultimately, the study's methodology and findings highlight the significance of looking beyond conventional research to comprehend the intricate genetic elements influencing cancer behavior. This makes it possible to conduct cancer genomics research using more comprehensive and innovative methods.

References

1. Abbas, M. and El-Manzalawy, Y. 2020. Machine learning based refined differential gene expression analysis of pediatric sepsis. BMC Medical Genomics 13(1). DOI: https://doi.org/10.1186/s12920-020-00771-4
2. Balagopalan, S., Ashok, S. and Mohandas, K.P. 2009. GSEA. Journal of Electrical Systems 5(4).
3. Behdenna, A., Colange, M., Haziza, J., Gema, A., Appé, G., Azencott, C.A. and Nordor, A. 2023. pyComBat, a Python tool for batch effects correction in high-throughput molecular data using empirical Bayes methods. BMC Bioinformatics 24(1). DOI: https://doi.org/10.1186/s12859-023-05578-5
4. Beroun, A., Mitra, S., Michaluk, P., Pijet, B., Stefaniuk, M. and Kaczmarek, L. 2019. MMPs in learning and memory and neuropsychiatric disorders. Cellular and Molecular Life Sciences 76(16). DOI: https://doi.org/10.1007/s00018-019-03180-8
5. Blighe, K., Rana, S. and Lewis, M. 2021. EnhancedVolcano version 1.10.0: Publication-ready volcano plots with enhanced colouring and labeling. R-Package.
6. Bro, R. and Smilde, A.K. 2014. Principal component analysis. Analytical Methods 6(9). DOI: https://doi.org/10.1039/c3ay41907j
7. Carbon, S. et al. 2017. Expansion of the gene ontology knowledgebase and resources: The gene ontology consortium. Nucleic Acids Research 45(D1). DOI: https://doi.org/10.1093/nar/gkw1108
8. Chollet, F. 2015. Keras: The Python Deep Learning library. Keras.Io.
9. Elgeldawi, E., Sayed, A., Galal, A.R. and Zaki, A.M. 2021. Hyperparameter tuning for machine learning algorithms used for arabic sentiment analysis. Informatics 8(4). DOI: https://doi.org/10.3390/informatics8040079
10. Ferreira, J.A. and Zwinderman, A.H. 2006. On the Benjamini-Hochberg method. Annals of Statistics 34(4). DOI: https://doi.org/10.1214/009053606000000425
11. Filus, K. and Domańska, J. 2023. Software vulnerabilities in TensorFlow-based deep learning applications. Computers and Security 124. DOI: https://doi.org/10.1016/j.cose.2022.102948
12. Guo, Y., Pan, W., Liu, S., Shen, Z., Xu, Y. and Hu, L. 2020. ERK/MAPK signalling pathway and tumorigenesis (Review). Experimental and Therapeutic Medicine. DOI: https://doi.org/10.3892/etm.2020.8454
13. Hadley Wickham, Romain François, Lionel Henry and Kirill Müller. 2020. A grammar of data manipulation [R package dplyr version 1.0.0].

14. Janizek, J.D. et al. 2023. PAUSE: principled feature attribution for unsupervised gene expression analysis. Genome Biology 24(1). DOI: https://doi.org/10.1186/s13059-023-02901-4

15. Jassal, B. et al. 2020. The reactome pathway knowledgebase. Nucleic Acids Research 48(D1). DOI: https://doi.org/10.1093/nar/gkz1031

16. Johansen, K.H., Golec, D.P., Okkenhaug, K. and Schwartzberg, P.L. 2023. Mind the GAP: RASA2 and RASA3 GTPase-activating proteins as gatekeepers of T cell activation and adhesion. Trends in Immunology 44(11). DOI: https://doi.org/10.1016/j.it.2023.09.002

17. Kanehisa, M., Furumichi, M., Sato, Y., Kawashima, M. and Ishiguro-Watanabe, M. 2023. KEGG for taxonomy-based analysis of pathways and genomes. Nucleic Acids Research 51(D1). DOI: https://doi.org/10.1093/nar/gkac963

18. Kassambara, A. and Mundt, F. 2020. factoextra: Extract and Visualize the Results of Multivariate Data Analyses. Package Version 1.0.7. R package version.

19. Lechner, M., Liu, J., Masterson, L. and Fenton, T.R. 2022. HPV-associated oropharyngeal cancer: epidemiology, molecular biology and clinical management. Nature Reviews Clinical Oncology 19(5). DOI: https://doi.org/10.1038/s41571-022-00603-7

20. Li, Z., Fang, R., Fang, J., He, S. and Liu, T. 2018. Functional implications of Rab27 GTPases in Cancer. Cell Communication and Signaling 16(1). DOI: https://doi.org/10.1186/s12964-018-0255-9

21. Li, Z., Fang, R., Fang, J., He, S. and Liu, T. 2018. Functional implications of Rab27 GTPases in Cancer. Cell Communication and Signaling 16(1). DOI: https://doi.org/10.1186/s12964-018-0255-9

22. Love, M.I., Huber, W. and Anders, S., 2014. Moderated estimation of fold change and dispersion for RNA-seq data with DESeq2. Genome Biology, 15(12), p.550. https://doi.org/10.1186/s13059-014-0550-8

23. Lu, C.W. et al. 2011. Overexpression of pyruvate dehydrogenase kinase 3 increases drug resistance and early recurrence in colon cancer. American Journal of Pathology 179(3). DOI: https://doi.org/10.1016/j.ajpath.2011.05.050

24. McKinney, W. 2011. pandas: a Foundational Python Library for Data Analysis and Statistics. Python for High Performance and Scientific Computing.

25. Mitra, R.S. et al. 2008. Rap1GAP promotes invasion via induction of matrix metalloproteinase 9 secretion, which is associated with poor survival in low N-stage

squamous cell carcinoma. Cancer Research 68(10). DOI: https://doi.org/10.1158/0008-5472.CAN-07-2755

26. Neumüller, O., Hoffmeister, M., Babica, J., Prelle, C., Gegenbauer, K. and Smolenski, A.P. 2009. Synaptotagmin-like protein 1 interacts with the GTPase-activating protein Rap1GAP2 and regulates dense granule secretion in platelets. Blood 114(7). DOI: https://doi.org/10.1182/blood-2008-05-155234

27. Pan, T., Zhao, J., Wu, W. and Yang, J. 2020. Learning imbalanced datasets based on SMOTE and Gaussian distribution. Information Sciences 512. DOI: https://doi.org/10.1016/j.ins.2019.10.048

28. Peterson, H., Kolberg, L., Raudvere, U., Kuzmin, I. and Vilo, J. 2020. gprofiler2 -- an R package for gene list functional enrichment analysis and namespace conversion toolset g: Profiler. F1000Research 9. DOI: https://doi.org/10.12688/f1000research.24956.2

29. Price, L.S., Hajdo-Milasinovic, A., Zhao, J., Zwartkruis, F.J.T., Collard, J.G. and Bos, J.L. 2004. Rap1 regulates E-cadherin-mediated cell-cell adhesion. Journal of Biological Chemistry 279(34). DOI: https://doi.org/10.1074/jbc.M404917200

30. Rampášek, L., Hidru, D., Smirnov, P., Haibe-Kains, B. and Goldenberg, A. 2019. Dr.VAE: Improving drug response prediction via modeling of drug perturbation effects. Bioinformatics 35(19). DOI: https://doi.org/10.1093/bioinformatics/btz158

31. Ri, J.H. and Kim, H. 2020. G-mean based extreme learning machine for imbalance learning. Digital Signal Processing: A Review Journal 98. DOI: https://doi.org/10.1016/j.dsp.2019.102637

32. Sabbatini, G. and Manganaro, L. 2023. On potential limitations of differential expression analysis with non-linear machine learning models. EMBnet.journal 28. DOI: https://doi.org/10.14806/ej.28.0.1035

33. Sinaga, K.P. and Yang, M.S. 2020. Unsupervised K-means clustering algorithm. IEEE Access 8. DOI: https://doi.org/10.1109/ACCESS.2020.2988796

34. Stekhoven, D.J. and Bühlmann, P. 2012. Missforest-Non-parametric missing value imputation for mixed-type data. Bioinformatics 28(1). DOI: https://doi.org/10.1093/bioinformatics/btr597

35. Sun, N. and Zhao, X. 2022. Therapeutic Implications of FABP4 in Cancer: An Emerging Target to Tackle Cancer. Frontiers in Pharmacology 13. DOI: https://doi.org/10.3389/fphar.2022.948610

36. Sundararajan, M., Taly, A. and Yan, Q. 2017. Axiomatic attribution for deep networks. In: 34th International Conference on Machine Learning, ICML 2017.

37. Tian, Y., Fan, B. and Wu, F. 2017. L2-Net: Deep learning of discriminative patch descriptor in Euclidean space. In: Proceedings - 30th IEEE Conference on Computer Vision and Pattern Recognition, CVPR 2017. DOI: https://doi.org/10.1109/CVPR.2017.649

38. Tolstikhin, I. et al. 2021. MLP-Mixer: An all-MLP Architecture for Vision. In: Advances in Neural Information Processing Systems.

39. Wang, Y., Xiao, Z. and Cao, G. 2022. A convolutional neural network method based on Adam optimizer with power-exponential learning rate for bearing fault diagnosis. Journal of Vibroengineering 24(4). DOI: https://doi.org/10.21595/jve.2022.22271

40. Waskom, M. 2021. seaborn: statistical data visualization. Journal of Open Source Software 6(60). DOI: https://doi.org/10.21105/joss.03021

41. Way, G.P., Zietz, M., Rubinetti, V., Himmelstein, D.S. and Greene, C.S. 2020. Compressing gene expression data using multiple latent space dimensionalities learns complementary biological representations. Genome Biology 21(1). DOI: https://doi.org/10.1186/s13059-020-02021-3

42. Wazery, Y.M., Saleh, M.E. and Ali, A.A. 2023. An optimized hybrid deep learning model based on word embeddings and statistical features for extractive summarization. Journal of King Saud University - Computer and Information Sciences 35(7). DOI: https://doi.org/10.1016/j.jksuci.2023.101614

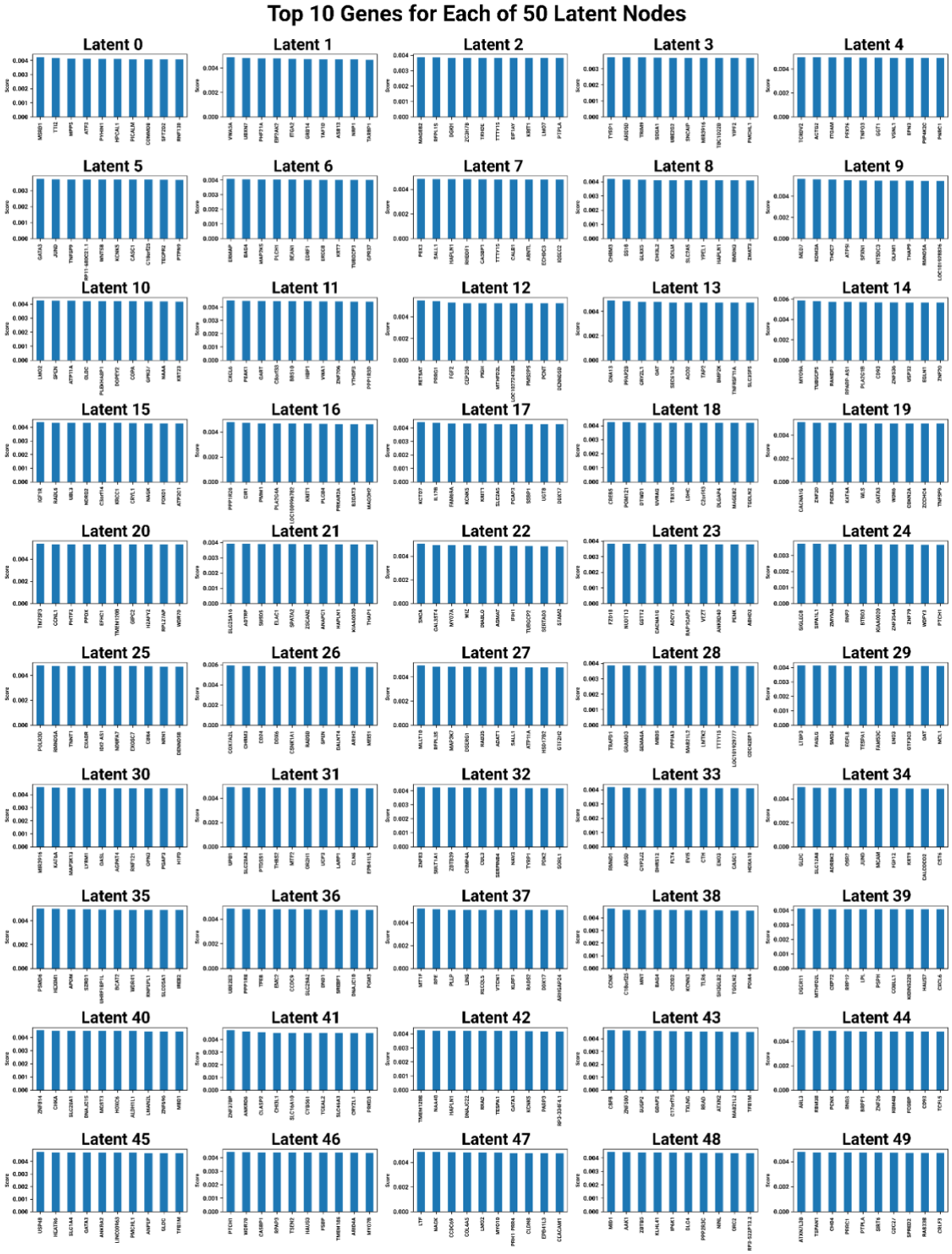
43. Wolf, F.A., Angerer, P. and Theis, F.J. 2018. SCANPY: Large-scale single-cell gene expression data analysis. Genome Biology 19(1). DOI: https://doi.org/10.1186/s13059-017-1382-0

44. Zhang, Y.L., Wang, R.C., Cheng, K., Ring, B.Z. and Su, L. 2017. Roles of Rap1 signaling in tumor cell migration and invasion. Cancer Biology and Medicine 14(1). DOI: https://doi.org/10.20892/j.issn.2095-3941.2016.0086

45. Zhang, Z. et al. 2006. Rap1GAP inhibits tumor growth in oropharyngeal squamous cell carcinoma. American Journal of Pathology 168(2). DOI: https://doi.org/10.2353/ajpath.2006.050132

Appendices

Appendix I


Top 10 Genes for Each of 50 Latent Nodes
Latent 0
Latent 1
Latent 2
Latent 3
Latent 4
Latent 5
Latent 6
Latent 7
Latent 8
Latent 9
Latent 10
Latent 11
Latent 12
Latent 13
Latent 14
Latent 15
Latent 16
Latent 17
Latent 18
Latent 19
Latent 20
Latent 21
Latent 22
Latent 23
Latent 24
Latent 25
Latent 26
Latent 27
Latent 28
Latent 29
Latent 30
Latent 31
Latent 32
Latent 33
Latent 34
Latent 35
Latent 36
Latent 37
Latent 38
Latent 39
Latent 40
Latent 41
Latent 42
Latent 43
Latent 44
Latent 45
Latent 46
Latent 47
Latent 48
Latent 49

Appendix II

Selected Latent Variable-Enriched Pathways

Pathway Name	P-value	Term Size	Query Size	Intersection	Precision	Recall	Latent Node
regulation of nervous system development	0.0236186136151001	457	16	5	0.3125	0.0109409190371991	7
DNA integration	0.0287922088818914	10	15	2	0.1333333333333333	0.2	9
Glucagon signaling pathway	0.0134641808035551	107	10	3	0.3	0.02803738317757	18
Cushing syndrome	0.0499569897009377	153	11	3	0.2727272727272727	0.0196078431372549	19
Vibrio cholerae infection	0.0246555455325596	50	6	2	0.3333333333333333	0.04	20
Golgi lumen acidification	0.0370534161963728	13	13	2	0.1538461538461538	0.1538461538461538	20
Cushing syndrome	0.0499569897009377	153	11	3	0.2727272727272727	0.0196078431372549	23
tRNA metabolic process	0.0414263692639973	210	18	4	0.2222222222222222	0.019047619047619	25
ECM-receptor interaction	0.0101450542933642	89	11	3	0.2727272727272727	0.0337078651685393	31
Glyoxylate and dicarboxylate metabolism	0.0121881807777088	30	7	2	0.2857142857142857	0.0666666666666666	34
cellular response to 2,3,7,8-tetrachlorodibenzo dioxine	0.0038484693649248	4	15	2	0.1333333333333333	0.5	41
response to 2,3,7,8-tetrachlorodibenzo dioxine	0.0179299300313183	8	15	2	0.1333333333333333	0.25	41
Base excision repair	0.0263601360727707	44	7	2	0.2857142857142857	0.0454545454545454	42
RNA degradation	0.0412133286559642	79	5	2	0.4	0.0253164556962025	43
neuromuscular junction development	0.0215300187657582	54	19	3	0.1578947368421052	0.0555555555555555	47
regulation of response to external stimulus	0.0390732084249658	1082	19	7	0.3684210526315789	0.0064695009242144	47

Appendix III

GSEA Info for Top 50 Pathways

Term	ES	NES	NOM p-val	FDR q-val	FWER p-val	Tag %	Gene %	latent
Ribosome	-0.2538932143878554	-3.142324180841197	0.0	0.0	0.0	64/112	30.62 %	0
Oxidative phosphorylation	-0.2407197097865659	-2.611673921650873	0.0	0.0	0.0	70/86	56.60 %	0
Thermogenesis	-0.158950904011502	-2.405693731233716	0.0	0.0	0.0	87/159	37.50 %	0
Taste transduction	-0.3048429308211678	-2.350171914030135	0.0	0.0	0.0	26/32	50.10 %	0
Epstein-Barr virus infection	0.0556416038563949	0.8350148290636356	0.6034482758620 69	1.0	1.0	115/179	59.99 %	0
Oxidative phosphorylation	0.1142496981063722	1.2249093076286393	0.1525423728813559	0.7361948188317199	1.0	52/86	50.47 %	1
Epstein-Barr virus infection	-0.0756836049783082	-1.1357622653143702	0.3448275862068966	0.6369253352905851	1.0	62/179	25.54 %	1
Thermogenesis	0.0748845499516672	1.0927577331087608	0.2948717948717949	0.8631416491166021	1.0	134/159	77.74 %	1
Ribosome	0.0936709992384217	1.0621660292973 25	0.3787878787878788	0.8778851648488162	1.0	24/112	13.53 %	1
Taste transduction	-0.1334816003429303	-0.9706323778105916	0.4444444444444444	0.7495123224441576	1.0	23/32	57.23 %	1
Ribosome	-0.3256476601525599	-4.022551650465103	0.0	0.0	0.0	82/112	40.25 %	2
Oxidative phosphorylation	-0.2609235596349908	-2.837492429056554	0.0	0.0	0.0	53/86	34.95 %	2
Epstein-Barr virus infection	-0.1484226108201942	-2.375236581547 1905	0.0	0.0057049714751426	0.06	88/179	33.48 %	2
Thermogenesis	-0.0882268099454029	-1.340207327255 8992	0.0975609756097561	0.2926098272734442	1.0	113/159	61.71 %	2
Taste transduction	-0.133293065125292	-0.923006243431 5842	0.4888888888888889	0.6908604815084033	1.0	13/32	26.30 %	2
Oxidative phosphorylation	-0.3275733015959381	-3.400119111390953	0.0	0.0	0.0	67/86	44.66 %	3
Ribosome	-0.2617170297897189	-3.286165938035 3325	0.0	0.0	0.0	87/112	51.10 %	3
Epstein-Barr virus infection	-0.1059999709738502	-1.862094830440 86	0.0	0.0579973024510487	0.56	88/179	37.69 %	3
Thermogenesis	-0.1212049069795281	-1.820560407417 6376	0.0	0.0682293846797823	0.64	72/159	32.36 %	3
Taste transduction	-0.2244361798488704	-1.517206705204 0372	0.0256410256410256	0.1659770744115658	1.0	14/32	19.96 %	3
Ribosome	-0.2232951808963537	-2.836444395628 6745	0.0	0.0	0.0	79/112	47.23 %	4
Oxidative phosphorylation	-0.1384100937509499	-1.484898203180035	0.025	0.3228428314904074	0.99	72/86	69.16 %	4
Taste transduction	-0.1599142914597349	-1.100229703388 3486	0.4193548387096774	0.6523335661482501	1.0	27/32	67.63 %	4
Thermogenesis	0.0627232772891256	0.8261903765388551	0.7179487179487 18	0.8583973003841902	1.0	139/159	82.01 %	4

Epstein-Barr virus infection	0.0475756092253786	0.6652826145585135	0.8552631578947368	0.9510038374797759	1.0	101/179	53.24 %	4
Epstein-Barr virus infection	-0.2321369172794	-3.8752412064043895	0.0	0.0	0.0	76/179	18.53 %	5
Ribosome	-0.2331264509898629	-3.037331039310221	0.0	0.0	0.0	87/112	53.96 %	5
Oxidative phosphorylation	-0.2113046485189271	-2.5688251815532457	0.0	0.0008765821089591	0.01	68/86	57.49 %	5
Thermogenesis	0.0767866793683777	1.1101762451219783	0.3225806451612903	1.0	1.0	136/159	78.48 %	5
Taste transduction	-0.1278100605290263	-0.8108845295541842	0.6666666666666666	0.8161653728339712	1.0	21/32	51.73 %	5
Ribosome	-0.3293229152882386	-4.450933710867719	0.0	0.0	0.0	68/112	27.16 %	6
Oxidative phosphorylation	-0.2803922514121083	-2.9523157014033363	0.0	0.0	0.0	70/86	52.93 %	6
Epstein-Barr virus infection	-0.1612168197723371	-2.83990224960349	0.0	0.0	0.0	80/179	27.60 %	6
Thermogenesis	-0.1045309528713468	-1.6119871628753508	0.0526315789473684	0.1086496401862565	0.98	102/159	52.93 %	6
Taste transduction	-0.0803663969469782	-0.5944365699407909	0.9473684210526316	0.950402144772118	1.0	22/32	59.83 %	6
Epstein-Barr virus infection	-0.1065109835343221	-1.744106362733484	0.0	0.1176882575158902	0.78	49/179	15.52 %	7
Ribosome	0.1120774229219907	1.279890247034121	0.1076923076923077	0.7245521177194651	1.0	58/112	42.30 %	7
Oxidative phosphorylation	0.108161573283124	1.119584501050699	0.3442622950819672	0.9349297823532704	1.0	75/86	77.11 %	7
Thermogenesis	0.0715029801756083	1.0268194922167353	0.463768115942029	0.9815923459967548	1.0	129/159	75.05 %	7
Taste transduction	0.1249958881658193	0.8067070959874992	0.6229508196721312	1.0	1.0	23/32	61.00 %	7
Thermogenesis	0.1367508982822331	1.9891285890048445	0.0	0.1958251871161404	0.47	88/159	42.83 %	8
Ribosome	0.1454806205398361	1.7462592473255552	0.0408163265306122	0.3844675970986771	0.87	84/112	61.29 %	8
Oxidative phosphorylation	0.1309589399054042	1.3715003663606282	0.0666666666666666	0.7863250756787104	1.0	31/86	24.00 %	8
Epstein-Barr virus infection	-0.0775275389761539	-1.2408344861416116	0.1379310344827586	0.4750103126804719	1.0	105/179	50.05 %	8
Taste transduction	-0.1302957666471551	-0.876358542353001	0.5769230769230769	0.8278352697259158	1.0	12/32	23.35 %	8
Thermogenesis	-0.1337794037804547	-2.100302981011935	0.0	0.0240763092961898	0.22	50/159	16.67 %	9
Oxidative phosphorylation	-0.1564861632838065	-1.6899188229068458	0.0	0.1199516123863745	0.88	29/86	16.56 %	9
Epstein-Barr virus infection	-0.0805443311691613	-1.3345202650671202	0.125	0.3780101242756428	1.0	74/179	31.81 %	9
Ribosome	-0.0944119478879425	-1.2113882241551532	0.2222222222222222	0.5218758215459836	1.0	24/112	10.81 %	9
Taste transduction	0.142512319190756	0.8988740228825484	0.5555555555555556	1.0	1.0	8/32	12.37 %	9
Ribosome	-0.1971230410161868	-2.6788469240337296	0.0	0.0025584472871636	0.01	72/112	43.60 %	10
Epstein-Barr virus infection	-0.1636372192150541	-2.540005734409352	0.0	0.0031980591089545	0.02	85/179	29.82 %	10
Oxidative phosphorylation	0.1500924419982399	1.5510957038556674	0.0307692307692307	0.3611661477497877	0.99	52/86	46.85 %	10
Thermogenesis	0.1123031774550938	1.5077141535503211	0.088235294117647	0.4161262137117119	0.99	90/159	46.85 %	10
Taste transduction	0.1335782743774241	0.8638481365202263	0.65625	0.9752898173595196	1.0	21/32	53.91 %	10

Epstein-Barr virus infection	-0.1548800515752707	-2.431047289293832	0.0	0.0014575470250698	0.01	82/179	28.95%	11
Oxidative phosphorylation	0.1182173254761076	1.1944193154577427	0.2622950819672131	0.6175221922037823	1.0	66/86	65.98%	11
Thermogenesis	0.0840036749263786	1.118619955095944	0.28125	0.6860132448708288	1.0	95/159	52.77%	11
Ribosome	-0.0782791132880562	-1.0479330673375782	0.3823529411764705	0.5760692258123907	1.0	71/112	54.18%	11
Taste transduction	-0.142353790073346	-0.9466568114068772	0.4883720930232558	0.7009968306571455	1.0	12/32	21.73%	11
Ribosome	-0.1590080895545469	-2.112035134935741	0.0	0.0280182897168985	0.25	82/112	56.27%	12
Oxidative phosphorylation	-0.1324742005360538	-1.461888415902940 4	0.0810810810810 81	0.2967726739750436	1.0	61/86	56.39%	12
Epstein-Barr virus infection	-0.0828798991794913	-1.306476902804451 2	0.1304347826086956	0.3912372091377831	1.0	61/179	24.35%	12
Taste transduction	-0.1640753539772809	-1.202076698646759 3	0.2285714285714285	0.4926908484063849	1.0	9/32	10.31%	12
Thermogenesis	0.0430498109286673	0.6098984184263628	0.9350649350649 35	1.0	1.0	138/159	83.46%	12
Thermogenesis	0.1106799758428105	1.552844450861132	0.1212121212121212	0.5010353563167 75	1.0	84/159	43.54%	13
Taste transduction	0.1898271430862881	1.238439155252835	0.2	0.8120975144105445	1.0	8/32	7.70%	13
Ribosome	0.1010080676659 86	1.158800145280816	0.2816901408450704	0.7224988615683561	1.0	57/112	42.36%	13
Oxidative phosphorylation	0.0893802743756362	0.9178164713944112	0.5151515151515151	0.7740193224552736	1.0	75/86	79.11%	13
Epstein-Barr virus infection	-0.0369440849574122	-0.5773223972275305	1.0	0.9895624758934112	1.0	162/179	86.23%	13
Ribosome	-0.2499602236106113	-3.402811022966832	0.0	0.0	0.0	70/112	36.31%	14
Oxidative phosphorylation	-0.2533110757351272	-2.882373363591102 4	0.0	0.0	0.0	58/86	40.98%	14
Epstein-Barr virus infection	-0.1403322253608299	-2.563615113060528	0.0	0.0026311111111111	0.01	89/179	34.09%	14
Thermogenesis	-0.0782485007267294	-1.125755033193022 2	0.2941176470588235	0.5246178861788618	1.0	110/159	60.17%	14
Taste transduction	0.1120801633981848	0.7121301279549598	0.8653846153846154	1.0	1.0	29/32	79.91%	14
Epstein-Barr virus infection	-0.1564731165548349	-2.623166779291232 3	0.0	0.0	0.0	58/179	15.80%	15
Oxidative phosphorylation	-0.1427779365221995	-1.545990268191191 7	0.0714285714285714	0.1606630509590157	1.0	45/86	37.13%	15
Ribosome	-0.0835052583452637	-1.045725824695814 3	0.4473684210526316	0.6350407605087761	1.0	64/112	47.89%	15
Thermogenesis	0.0685810193717143	0.9241792850269684	0.609375	0.9146829405107706	1.0	86/159	48.40%	15
Taste transduction	-0.1089751365711126	-0.8046743421424567	0.7021276595744681	0.858769141421 02	1.0	22/32	56.79%	15
Oxidative phosphorylation	-0.1934690155536926	-2.257917143682 82	0.0	0.0135284910529 21	0.1	70/86	61.20%	16
Thermogenesis	-0.1199857130176 65	-2.059011466760391	0.0	0.0243252675663099	0.25	118/159	61.23%	16
Ribosome	-0.0986916187640376	-1.234305579962574 8	0.2413793103448276	0.5549282964592411	1.0	93/112	72.43%	16
Epstein-Barr virus infection	-0.0735439406826843	-1.201014151375782 2	0.25	0.5515253606328525	1.0	121/179	59.04%	16
Taste transduction	-0.1417973572809813	-0.923938637672024 4	0.6538461538461539	0.8495865697820095	1.0	15/32	31.04%	16

Ribosome	-0.14298434144614468	-1.935132220388343	0.0	0.0402945619335347	0.44	86/112	61.80%	17
Epstein-Barr virus infection	-0.0989803694223771	-1.6377537736470795	0.0	0.1405948784347576	0.95	86/179	37.03%	17
Oxidative phosphorylation	-0.1321516800386444	-1.5503137660883377	0.0294117647058823	0.1873047842836362	0.98	47/86	40.21%	17
Thermogenesis	-0.0495010447489337	-0.753272068712083	0.8709677419354839	0.9325568175837132	1.0	80/159	44.25%	17
Taste transduction	0.0837504809450444	0.5391166734889357	1.0	0.9862752920198 86	1.0	18/32	49.33%	17
Ribosome	-0.2300643695538789	-3.032637747261451	0.0	0.0	0.0	67/112	36.08%	18
Oxidative phosphorylation	-0.2258420027873637	-2.426969664198208	0.0	0.0030002293168904	0.03	61/86	47.80%	18
Epstein-Barr virus infection	-0.163436713082365	-2.312736020117996	0.0	0.0060671303963784	0.07	66/179	19.74%	18
Thermogenesis	-0.0540860555409017	-0.8808549381934389	0.6428571428571429	0.7158308325876414	1.0	137/159	80.28%	18
Taste transduction	0.0903422763299656	0.5715602775591783	0.9423076923076924	0.9854396948327132	1.0	12/32	29.38%	18
Ribosome	-0.2865315189205287	-3.5741418374315392	0.0	0.0	0.0	80/112	41.74%	19
Oxidative phosphorylation	-0.228410490583011	-2.4631593708013453	0.0	0.0	0.0	40/86	22.24%	19
Epstein-Barr virus infection	-0.1084580718550667	-1.9171496093342697	0.0	0.0473985890652557	0.4	77/179	30.61%	19
Thermogenesis	-0.0895152851569006	-1.32764710460203	0.1363636363636363	0.420344560588463	1.0	132/159	73.22%	19
Taste transduction	0.1926586094746618	1.1079070707887402	0.3859649122807017	0.8063496076781 06	1.0	30/32	74.82%	19
Epstein-Barr virus infection	-0.0853369011310599	-1.5479124740309584	0.0303030303030303	0.2999792957090357	0.97	46/179	15.94%	20
Ribosome	-0.1077871147797501	-1.3732178053318371	0.0666666666666666	0.3707169657065273	1.0	59/112	40.58%	20
Taste transduction	-0.147339358915744	-1.0153596695405562	0.4722222222222222	0.6979608190464 14	1.0	12/32	21.09%	20
Thermogenesis	0.0542222308163235	0.7571389446423754	0.7866666666666666	0.9763971347870776	1.0	150/159	89.39%	20
Oxidative phosphorylation	0.0704483502934994	0.7206262365493948	0.8235294117647058	0.9541908068839632	1.0	84/86	90.89%	20
Ribosome	0.227543804362252	2.561665516577705	0.0	0.0061374558508482	0.01	72/112	42.71%	21
Epstein-Barr virus infection	-0.1441302848400509	-2.324946604635544	0.0	0.0037351456909816	0.05	112/179	47.05%	21
Taste transduction	0.2050893693918116	1.3499798123440814	0.1639344262295081	1.0	1.0	31/32	76.55%	21
Oxidative phosphorylation	-0.11407752268435	-1.2261204071398637	0.2258064516129032	0.3921902975530735	1.0	28/86	20.10%	21
Thermogenesis	-0.0423312481418022	-0.7048522598483786	0.935483870967742	0.919570897674442	1.0	152/159	91.18%	21
Epstein-Barr virus infection	-0.104099107261312	-1.5395196576693624	0.08	0.137222527976518	0.99	38/179	9.71%	22
Ribosome	-0.1188469970281153	-1.5179883663741862	0.0666666666666666	0.1478504771584324	0.99	32/112	15.52%	22
Oxidative phosphorylation	-0.1063207806531286	-1.2234510409142016	0.1666666666666666	0.3499987708812442	1.0	64/86	62.78%	22
Taste transduction	-0.1162346220625998	-0.8115098576982108	0.6571428571428571	0.7833040746558256	1.0	17/32	39.94%	22
Thermogenesis	0.0308342620424767	0.4293938133054199	1.0	0.9970842273202398	1.0	29/159	16.15%	22

Epstein-Barr virus infection	-0.14902221257943 51	-2.45171988953616 14	0.0	0.00814407914514 49	0.04	94/179	36.77 %	23
Oxidative phosphorylation	-0.19005011237156 08	-1.90931018117637 9	0.0	0.04703205706321 22	0.42	71/86	63.12 %	23
Taste transduction	-0.18159682665249 49	-1.30095341034467 85	0.14285714285714 28	0.34879753891035 11	1.0	10/32	12.03 %	23
Thermogenesis	-0.07556885467242 18	-1.08327497437372 18	0.30303030303030 3	0.52083931157935 02	1.0	61/159	29.92 %	23
Ribosome	0.05200799950858 84	0.64139179465484	0.86792452830188 68	0.95542507068300 7	1.0	53/112	43.18 %	23
Oxidative phosphorylation	-0.21400883420069 68	-2.55811590533719 45	0.0	0.00101422284433 16	0.01	46/86	31.19 %	24
Epstein-Barr virus infection	-0.15804110437355 01	-2.55027808220968 5	0.0	0.00094660798804 28	0.01	60/179	16.72 %	24
Taste transduction	-0.19073659198254 91	-1.29392741586276 4	0.21568627450980 39	0.31429512411984 39	1.0	17/32	32.98 %	24
Ribosome	-0.08603412489103 68	-1.10049742358176 73	0.31034482758620 69	0.48152453707547 95	1.0	106/112	85.90 %	24
Thermogenesis	-0.07114139568919 96	-1.07512667044882 25	0.33333333333333 3	0.50777023358606 02	1.0	117/159	65.75 %	24
Thermogenesis	0.16596227416112 06	2.24675356343695 44	0.0	0.04113522537562 6	0.17	116/159	57.68 %	25
Oxidative phosphorylation	0.18887235102240 7	2.16657864955916 5	0.0	0.04674457429048 41	0.25	40/86	29.28 %	25
Ribosome	-0.15653381984746 87	-1.86072528028656 4	0.02857142857142 85	0.12904200664853 43	0.64	69/112	44.77 %	25
Taste transduction	-0.16654150025725 6	-1.24175140948935 85	0.14893617021276 59	0.58704895738893 94	1.0	11/32	16.31 %	25
Epstein-Barr virus infection	-0.04714928581694 78	-0.75321157282696 6	0.88888888888888 88	0.95724711183720 36	1.0	148/179	77.11 %	25
Epstein-Barr virus infection	-0.11202983408140 06	-2.01460724246159 37	0.0	0.02528613683127 57	0.23	103/179	44.77 %	26
Oxidative phosphorylation	-0.16097193256261 07	-1.70468333402446 54	0.03125	0.10787657076719 57	0.75	44/86	33.41 %	26
Ribosome	-0.10616454174195 38	-1.36429966939886 05	0.15	0.33130586098251 03	1.0	73/112	53.04 %	26
Taste transduction	0.15921933866926 86	1.04582504830761 12	0.34615384615384 61	0.96160150934059 12	1.0	10/32	17.21 %	26
Thermogenesis	0.05634979117132 77	0.73600086397414 72	0.82608695652173 91	0.95764728947620 56	1.0	90/159	52.59 %	26
Ribosome	-0.19648143374535 77	-2.49636961994187 7	0.0	0.0	0.0	89/112	58.81 %	27
Epstein-Barr virus infection	-0.12273966725179 17	-2.37732596646043 2	0.0	0.00354333311297 67	0.02	102/179	42.99 %	27
Taste transduction	-0.11620510893420 8	-0.84348161321455 62	0.64150943396226 41	0.76772726547415 8	1.0	11/32	21.36 %	27
Thermogenesis	0.05490775164211 73	0.71688940367332 95	0.84126984126984 13	0.90687528137844 74	1.0	62/159	35.14 %	27
Oxidative phosphorylation	-0.06157413739958 72	-0.64778043769912 24	0.91176470588235 28	0.95223643948932 63	1.0	33/86	30.82 %	27
Epstein-Barr virus infection	-0.16551894743825 41	-2.87095822691745 2	0.0	0.0	0.0	77/179	25.63 %	28
Ribosome	-0.20690166767475 44	-2.80023267670819 5	0.0	0.0	0.0	80/112	50.28 %	28
Thermogenesis	0.13131576898291 46	1.88494187185635	0.0	0.46252793043058 16	0.67	110/159	56.99 %	28
Taste transduction	-0.14716004955732 11	-0.99818353644803 96	0.39130434782608 7	0.65225196259679 02	1.0	30/32	78.87 %	28
Oxidative phosphorylation	-0.07193954001725 45	-0.79483742357533 43	0.7	0.85825781901099 5	1.0	85/86	91.65 %	28

Ribosome	-0.3640114664957908	-4.447733367143593	0.0	0.0	0.0	77/112	31.66%	29
Oxidative phosphorylation	-0.2743933145830459	-3.267497189735176	0.0	0.0	0.0	57/86	37.99%	29
Thermogenesis	-0.1322448508758917	-2.085066924759269	0.02272727272727272	0.0196933560477001	0.24	96/159	46.08%	29
Epstein-Barr virus infection	0.09191624785055 91	1.263728815180344 3	0.15714285714285 71	0.53933073492749 04	1.0	58/179	24.48%	29
Taste transduction	-0.1409379951415683	-0.949507222430678 4	0.6	0.9666477380276356	1.0	15/32	31.53%	29
Oxidative phosphorylation	-0.2601385384155186	-3.008403321908917	0.0	0.0	0.0	69/86	53.33%	30
Ribosome	-0.2225102822614033	-2.936879735534422 5	0.0	0.0	0.0	73/112	41.60%	30
Thermogenesis	-0.1091719810812835	-1.721818173594800 6	0.0	0.0964372318597276	0.76	114/159	59.59%	30
Taste transduction	-0.1681589880592587	-1.189226138480616 9	0.2325581395348837	0.4385299727053663	1.0	26/32	63.47%	30
Epstein-Barr virus infection	0.05570836015450 44	0.843336333692220 6	0.625	0.7871948695747323	1.0	25/179	9.59%	30
Ribosome	-0.3088603817864165	-4.509509091359980 5	0.0	0.0	0.0	67/112	27.76%	31
Oxidative phosphorylation	-0.2280577290437473	-2.633010961111174	0.0	0.0067149673087117	0.03	46/86	29.19%	31
Thermogenesis	-0.1089243720432984	-1.611895997137293 7	0.03571428571428 57	0.17650771211470 98	0.94	58/159	24.24%	31
Taste transduction	0.16921504518039 77	1.121216782531937 7	0.26666666666666 66	1.0	1.0	8/32	9.57%	31
Epstein-Barr virus infection	-0.0540938598818739	-0.887680072442927 9	0.5625	0.8275281530626998	1.0	108/179	53.43%	31
Ribosome	-0.2578530355840409	-3.329316745057 25	0.0	0.0	0.0	51/112	18.35%	32
Oxidative phosphorylation	-0.3010482068914579	-3.251304941949133	0.0	0.0	0.0	55/86	32.65%	32
Thermogenesis	-0.1950881150434 57	-3.146093908137929 3	0.0	0.0	0.0	84/159	31.91%	32
Taste transduction	-0.1598448791793256	-1.149961480762 5744	0.2391304347826087	0.5808088388094853	1.0	9/32	10.34%	32
Epstein-Barr virus infection	0.04304922002131 03	0.636513713305330 1	0.8985507246376812	0.9827247306416328	1.0	116/179	61.99%	32
Ribosome	-0.3630708010063278	-4.739782665252094	0.0	0.0	0.0	85/112	39.11%	33
Oxidative phosphorylation	-0.3017187042155527	-3.166046240333104	0.0	0.0	0.0	70/86	50.74%	33
Thermogenesis	-0.1383763649312712	-2.030776858527007	0.0	0.0216223562388516	0.33	107/159	52.73%	33
Epstein-Barr virus infection	-0.1147388570848083	-1.731023342971171	0.03448275862068 96	0.0902363833497384	0.8	68/179	25.48%	33
Taste transduction	-0.2120107719433776	-1.489015373061367 45	0.0980392156862745	0.2118406523401002	0.99	14/32	21.31%	33
Oxidative phosphorylation	-0.2545196538658869	-2.853425457553988	0.0	0.0	0.0	59/86	41.96%	34
Epstein-Barr virus infection	-0.1406276819473865	-2.199380839754852	0.0	0.0069618490671122	0.08	101/179	40.64%	34
Ribosome	-0.1404734864995973	-1.695817266937874 4	0.0	0.0890740364424574	0.86	55/112	33.62%	34

Taste transduction	-0.1327015686283943	-0.9523420525198376	0.4772727272727273	0.6694432158828444	1.0	8/32	10.41%	34
Thermogenesis	-0.0642275325875987	-0.9438060795186816	0.5121951219512195	0.6694621168305378	1.0	46/159	21.19%	34
Epstein-Barr virus infection	-0.1337794321853186	-2.1911135547340184	0.0	0.0103028113374597	0.14	66/179	22.07%	35
Thermogenesis	0.1169191327605175	1.5391984192601724	0.0422535211267605	0.8218183832899328	1.0	88/159	45.25%	35
Oxidative phosphorylation	0.0975026009723607	1.0324645616114798	0.4	0.9667967358698148	1.0	53/86	53.19%	35
Taste transduction	-0.1216536857868528	-0.8727845560307057	0.5957446808510638	0.7538368738593555	1.0	19/32	45.99%	35
Ribosome	-0.0485747667164141	-0.5931017707095675	0.9393939393939394	0.9753651291582288	1.0	84/112	69.03%	35
Oxidative phosphorylation	-0.2263274299523434	-2.737231883792341	0.0	0.0	0.0	64/86	50.58%	36
Thermogenesis	-0.1201911536898513	-1.9299521792350136	0.0	0.0538910872432636	0.44	93/159	44.78%	36
Taste transduction	0.211778769747215	1.3365944361544937	0.173076923076923	0.5778762826788498	1.0	24/32	55.02%	36
Ribosome	-0.1034471847868074	-1.2945477592320158	0.125	0.3413102192073362	1.0	49/112	31.63%	36
Epstein-Barr virus infection	-0.0576208425867244	-0.9646737080773496	0.5	0.7001758683499778	1.0	43/179	16.70%	36
Ribosome	-0.2780402190998905	-3.7626702164566943	0.0	0.0	0.0	80/112	42.60%	37
Oxidative phosphorylation	-0.1833048188200864	-2.050333616747916	0.0	0.0303655660377358	0.28	76/86	69.50%	37
Epstein-Barr virus infection	-0.0958088948657161	-1.629439063271938	0.0	0.1462421909509686	0.86	102/179	46.10%	37
Thermogenesis	-0.0836067027722523	-1.3190298606653903	0.1666666666666666	0.3955309627479438	1.0	152/159	87.09%	37
Taste transduction	0.1273989683571168	0.8722501590968771	0.576271186440678	0.7863051117965717	1.0	6/32	7.30%	37
Thermogenesis	0.1543315294185555	2.100021315152871	0.0149253731343283	0.2416159380188157	0.42	97/159	47.08%	38
Ribosome	-0.1395500689620349	-2.0428100405841603	0.0	0.0313967673071058	0.19	88/112	63.77%	38
Epstein-Barr virus infection	-0.0968682231117353	-1.5861196199728786	0.0	0.1635434045530038	0.91	48/179	15.98%	38
Oxidative phosphorylation	0.1404503366589868	1.4065092972713316	0.1166666666666666	0.7813613724405091	1.0	51/86	46.79%	38
Taste transduction	-0.1333043674603921	-0.933825652743302	0.5853658536585366	0.7637583520474647	1.0	23/32	57.40%	38
Epstein-Barr virus infection	-0.1208544640341385	-1.8792193758859483	0.0	0.0779192913084126	0.6	71/179	26.75%	39
Ribosome	-0.1214087761786404	-1.6738897666231272	0.0277777777777777	0.1330911766058209	0.86	64/112	44.26%	39
Oxidative phosphorylation	-0.1337418025070802	-1.4844452740123826	0.0909090909090909	0.2296105568072095	0.98	66/86	62.70%	39
Taste transduction	-0.1912523199587957	-1.3816456726391608	0.1333333333333333	0.3064158024799114	1.0	13/32	20.46%	39
Thermogenesis	0.0383834139505656	0.5746257618987081	0.9696969696969696	1.0	1.0	140/159	84.73%	39
Ribosome	-0.1330614426196696	-1.6552021458471902	0.0476190476190476	0.1990882759126407	0.9	96/112	71.95%	40
Taste transduction	-0.1995615584775341	-1.532337126571576	0.0465116279069767	0.2384375715795661	1.0	9/32	6.79%	40

Oxidative phosphorylation	-0.1128483370623297	-1.2799354987414728	0.1707317073170731	0.3859904273473485	1.0	50/86	45.85%	40
Thermogenesis	-0.0698022490763607	-0.9963950374822887	0.4615384615384615	0.6727154407149333	1.0	47/159	21.68%	40
Epstein-Barr virus infection	-0.0423759172324384	-0.6557109849000161	0.9333333333333332	0.9560671357686714	1.0	36/179	15.15%	40
Oxidative phosphorylation	-0.3178452567996256	-3.2308443138546794	0.0	0.0	0.0	60/86	36.90%	41
Ribosome	-0.2398031423342298	-3.2183620427351154	0.0	0.0	0.0	62/112	29.85%	41
Epstein-Barr virus infection	-0.0925176446724106	-1.5139748150739774	0.0714285714285714	0.1867903688977247	1.0	94/179	41.80%	41
Thermogenesis	-0.0858185058777302	-1.2891483325508557	0.1388888888888889	0.362055310413939	1.0	73/159	35.91%	41
Taste transduction	0.1355329698643851	0.9167825200406078	0.6101694915254238	0.8683607535453032	1.0	11/32	22.45%	41
Ribosome	-0.1640123151182866	-2.203301450185885	0.0	0.0058554195650259	0.03	47/112	24.40%	42
Epstein-Barr virus infection	-0.1240266084660245	-2.058553522884664	0.0	0.0156144521734026	0.12	58/179	18.85%	42
Oxidative phosphorylation	-0.1371541527892488	-1.525522447158714	0.0789473684210526	0.164211988690284	0.99	31/86	21.18%	42
Thermogenesis	0.0720718234332094	1.0664691857698492	0.4	0.6857369966176559	1.0	76/159	41.91%	42
Taste transduction	0.1515671345565241	1.030931393872168	0.4230769230769231	0.7313310413885615	1.0	18/32	42.56%	42
Oxidative phosphorylation	-0.2727001833743558	-3.240032787152209	0.0	0.0	0.0	61/86	42.59%	43
Ribosome	-0.2035206597539268	-2.6583790691907123	0.0	0.0	0.0	54/112	26.37%	43
Epstein-Barr virus infection	-0.1166104695400355	-1.923537561138284	0.0	0.0455769077000986	0.48	63/179	22.09%	43
Thermogenesis	-0.1254676352054362	-1.845754742062561	0.0	0.0558676937018577	0.64	118/159	60.51%	43
Taste transduction	-0.0841319508329352	-0.5943039962466512	0.9310344827586208	0.9839238785681922	1.0	5/32	6.19%	43
Oxidative phosphorylation	-0.2321417570446411	-2.608379742905366	0.0	0.0050045703839122	0.03	45/86	27.77%	44
Thermogenesis	-0.1553811792791847	-2.413857190150817	0.0	0.0033363802559414	0.03	73/159	29.10%	44
Epstein-Barr virus infection	-0.0995353249186391	-1.777463698855575	0.0	0.0973110907982937	0.78	65/179	24.97%	44
Ribosome	-0.0827061919968607	-1.1703424936817148	0.1891891891891892	0.5609355503322596	1.0	94/112	74.95%	44
Taste transduction	-0.1152252573035539	-0.7379242450079108	0.8333333333333334	0.9559267559120128	1.0	18/32	43.30%	44
Epstein-Barr virus infection	-0.1483740711922618	-2.5401627938768514	0.0	0.0028021015761821	0.01	94/179	36.32%	45
Ribosome	-0.1752683634281028	-2.1107840486152813	0.0	0.0196147110332749	0.12	104/112	75.04%	45
Thermogenesis	-0.0971470308528347	-1.6584616343711849	0.0344827586206896	0.1473697865992086	0.9	91/159	46.24%	45
Oxidative phosphorylation	-0.1096084072672724	-1.2988032557097435	0.1481481481481481	0.4687428614939465	1.0	33/86	26.02%	45
Taste transduction	-0.1551495073391745	-1.0785825390232742	0.3076923076923077	0.6719363847209733	1.0	20/32	45.38%	45
Ribosome	-0.1431119957761128	-1.872286502984436	0.0	0.0499218630888855	0.55	73/112	49.78%	46

Epstein-Barr virus infection	-0.0793189315278572	-1.3118898412789644	0.1481481481481481	0.2911412835816963	1.0	123/179	59.66%	46
Thermogenesis	0.0936037460391565	1.2548579471203485	0.1969696969696969	1.0	1.0	111/159	61.67%	46
Oxidative phosphorylation	0.0813586157156401	0.8352347040497169	0.6470588235294118	0.9734071341051324	1.0	59/86	61.67%	46
Taste transduction	-0.0950583728437162	-0.6570628315004804	0.8235294117647058	0.9181045592912 36	1.0	26/32	70.77%	46
Epstein-Barr virus infection	-0.1052548510684108	-1.6942473121961907	0.0	0.1527238882643749	0.83	70/179	27.11%	47
Taste transduction	-0.1665622841165926	-1.1589575677115576	0.1578947368421052	0.5307371527555014	1.0	27/32	66.92%	47
Ribosome	0.0928670008454053	1.0481938467277976	0.3174603174603174	0.9726296283829868	1.0	60/112	46.00%	47
Oxidative phosphorylation	0.0764689987773298	0.8349208881250927	0.6190476190476191	0.9295712285133726	1.0	27/86	25.32%	47
Thermogenesis	0.0516962539223096	0.6632178111894441	0.8947368421052632	0.9660380807615692	1.0	77/159	44.90%	47
Ribosome	-0.2086899163590077	-2.8344373214639305	0.0	0.0	0.0	92/112	60.70%	48
Oxidative phosphorylation	-0.1847751109308437	-2.0669629644262 6	0.0	0.0289672920968369	0.27	57/86	46.54%	48
Taste transduction	-0.2350461769872571	-1.5705780859429173	0.0344827586206896	0.2290226531406 17	0.97	17/32	27.56%	48
Epstein-Barr virus infection	-0.0873852347574 65	-1.4178785746948572	0.0625	0.3207701610135031	1.0	53/179	19.58%	48
Thermogenesis	0.0805316014676845	1.1124624427720406	0.2876712328767123	0.7825594377496813	1.0	56/159	28.71%	48
Oxidative phosphorylation	-0.2510168501713146	-2.7585729333414672	0.0	0.0094270547318323	0.01	61/86	44.79%	49
Thermogenesis	-0.0826014889987527	-1.4245942022814 24	0.0	0.3296102350879946	1.0	85/159	43.73%	49
Epstein-Barr virus infection	0.1011614267036261	1.4215808102880614	0.1111111111111111	0.4581956717621208	1.0	46/179	17.31%	49
Taste transduction	-0.1487174195437644	-1.1160397511139348	0.35	0.6191689547867472	1.0	20/32	46.14%	49
Ribosome	-0.0626830455571333	-0.8321608130739544	0.6756756756756757	0.9056015526361488	1.0	109/112	90.87%	49

Appendix IV

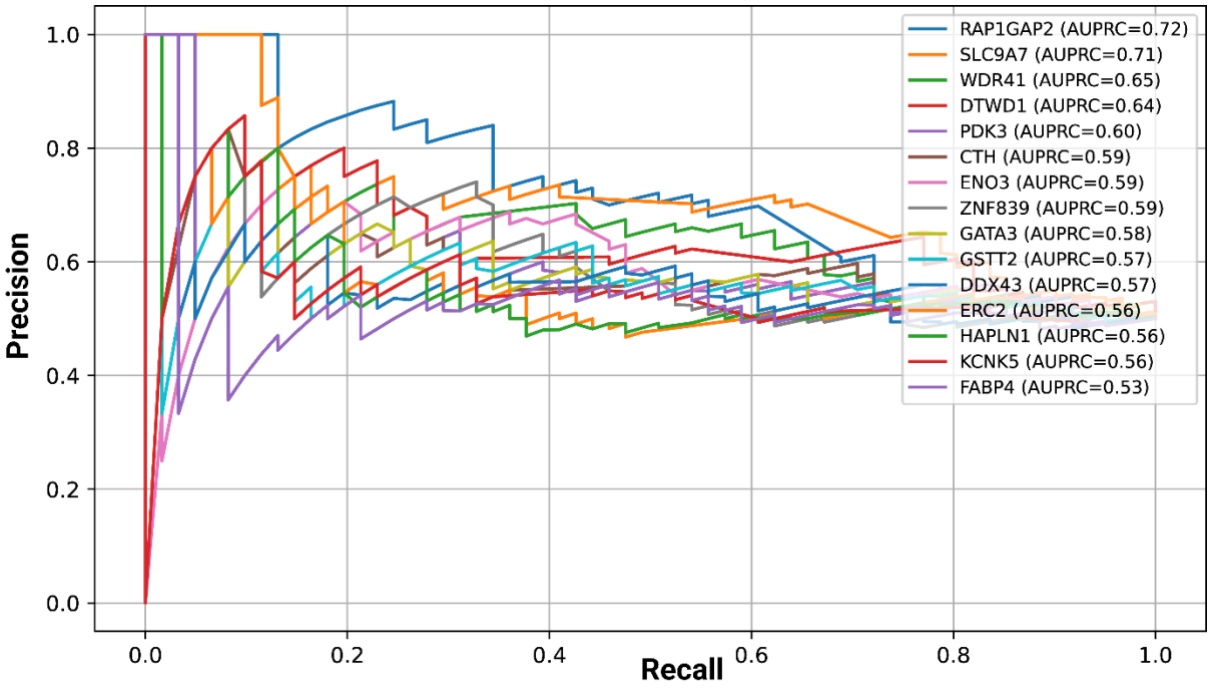


Figure Appendix IV: Precision–recall curves for the top 15 latent-space-contributing genes.

Appendix V

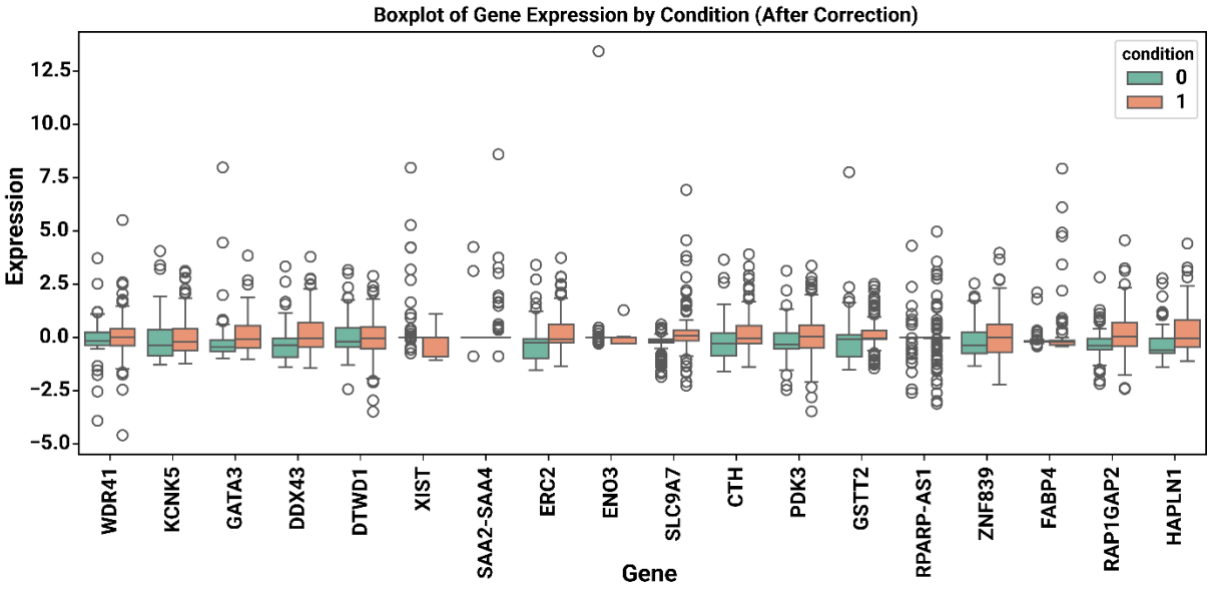


Figure Appendix V: Boxplot of gene expression levels for the top latent contributors across tumor (1) and control (0) conditions